Title: Arctic and Antarctic sea ice mean state in the Community Earth System Model Version 2 and the influence of atmospheric chemistry

Authors: Alice K. DuVivier[1], Marika M. Holland[1], Jennifer E. Kay[2], Simone Tilmes[1], Andrew Gettelman[1], David A. Bailey[1]

[1] National Center for Atmospheric Research, Boulder, CO

[2] Department of Atmospheric and Oceanic Sciences and Cooperative Institute for Research in Environmental Sciences, University of Colorado at Boulder, Boulder, CO

Date of re-submission:

July 2020, JGR-Oceans

Corresponding author:

Alice K. DuVivier, CGD, P.O. Box 3000, Boulder, CO 80307

Email: duvivier@ucar.edu

Key Points:

1. Simulated sea ice matches Arctic and Antarctic observed mean extent and volume, and Arctic observed historic trends.
2. The Arctic sea ice state differs significantly in two model configurations from cloud-aerosol chemistry impacts on surface radiation.
3. Seasonality of Arctic liquid clouds drives differences in the ice-albedo feedback and the amount of summer ice loss.

Abstract

Arctic and Antarctic sea ice has undergone significant and rapid change with the changing climate. Here, we present preindustrial and historical results from the newly released Community Earth System Model Version 2 (CESM2) to assess the Arctic and Antarctic sea ice. Two configurations of the CESM2 are available that differ only in their atmospheric model top and the inclusion of comprehensive atmospheric chemistry, including prognostic aerosols. The CESM2 configuration with comprehensive atmospheric chemistry has significantly thicker Arctic sea ice year-round and better captures decreasing trends in sea ice extent and volume over the satellite period. In the Antarctic, both CESM configurations have similar mean state ice extent and volume, but the ice extent trends are opposite to satellite observations. We find that differences in the Arctic sea ice between CESM2 configurations are the result of differences in liquid clouds. Over the Arctic, the CESM2 configuration without prognostic aerosol formation has fewer aerosols to form cloud condensation nuclei, leading to thinner liquid clouds. As a result, the sea ice receives much more shortwave radiation early in the melt season, driving a stronger ice-albedo feedback and leading to additional sea ice loss and significantly thinner ice year-round. The aerosols necessary for the Arctic liquid cloud formation are produced from different precursor emissions and transported to the Arctic. Thus, the main reason sea ice differs in the Arctic is due to the transport of cloud-impacting aerosols into the region, while the Antarctic remains relatively pristine from extra-polar aerosol transport.

Plain Language Summary

Arctic and Antarctic sea ice has undergone significant and rapid change with the changing climate. Here we assess Arctic and Antarctic sea ice in a new state-of-the-art Earth System Model, the Community Earth System Model Version 2 (CESM2). In particular, we explore how the atmosphere impacts the sea ice. When the CESM2 model does not include chemistry of particles in the atmosphere, we find that Arctic clouds are thinner, which allows more sunlight to reach the sea ice at the surface in the spring and summer. As a result, the sea ice melts more so that it covers less of the Arctic Ocean surface and is overall thinner than in CESM2 simulations that do include chemistry of particles. In contrast, inclusion or lack of particle chemistry does not lead to large differences in the Antarctic sea ice thickness or surface area covered by sea ice. The reason for the opposite results in the hemispheres is that the particles that impact clouds are produced outside the Arctic and Antarctic. These particles are transported successfully to the Arctic, but the Antarctic remains relatively pristine from external particle transport.

1. Introduction

Recent rapid and substantial changes in the polar regions include warming oceans and transformation of the Arctic and Antarctic sea ice cover (Meredith et al., 2019; Parkinson, 2019). The Arctic sea ice cover has become thinner (Lindsay & Schweiger, 2015; Kwok, 2018) and less extensive (Stroeve & Notz, 2018). Satellite observations since 1979 show that decreases in Arctic sea ice extent occur in all months, and all minima since the large loss of sea ice in 2007 have been lower than anything seen before 2007 (Richter-Menge et al., 2019). In the Antarctic, after decades of increasing Antarctic sea ice extent, there was a dramatic decrease in ice extent in 2016 (Stuecker et al., 2017; J. Turner et al., 2017; Meehl et al., 2019; Parkinson, 2019).

In the Earth system, changes to sea ice have the capacity to impact local boundary layer clouds, temperature, and humidity, which can feed back on sea ice evolution (Kay & Gettelman, 2009; Boisvert & Stroeve, 2015; Morrison et al., 2018; Huang et al., 2019) and the large-scale atmospheric circulation (e.g., Alexander, 2004; Barnes & Screen, 2015; Deser et al., 2016). Changing sea ice impacts ecosystems and human infrastructure (Hunter et al., 2010; Kovacs et al., 2011; Jenouvrier et al., 2014; Moon et al., 2019). In order to assess possible future sea ice changes and their impacts with confidence, we must evaluate our historical climate model representations of the sea ice state as well as their representation of variability and trends.

The Community Earth System Model (CESM) and its various iterations have been used widely to understand the changing Arctic and Antarctic. Recent work has highlighted the impact of internal climate variability on the possible range of Arctic and Antarctic sea ice conditions (e.g., Mahlstein et al., 2013; Swart et al., 2015; Jahn et al., 2016). Previous versions of the CESM have performed well in capturing the Arctic mean sea ice state, trends, and variability (e.g., Holland et al., 2006; Kay et al., 2011a; Jahn et al., 2012; Barnhart et al., 2015; Jahn et al., 2016; DeRepentigny et al., 2016; Labe et al., 2018). In the Antarctic, however, previous versions of CESM have too extensive sea ice cover and are unable to replicate observed trends in sea ice extent, even when accounting for potential effects of internal variability (Landrum et al., 2012; Mahlstein et al., 2013). Indeed, no CMIP5 model has replicated the observed trends of increasing Antarctic sea ice extent (Polvani & Smith, 2013; J. Turner et al., 2013; Shu et al., 2015). Additionally, extensive work has been done to assess the impact of clouds on Arctic climate change and place cloud feedbacks in the context of other processes and feedbacks (e.g., Kay et al., 2012; Pithan & Mauritsen, 2014; Goosse et al., 2018). Detailed process-level assessment is essential to understand the contribution of clouds to simulated Arctic change in models and assess their realism. Some versions of the atmospheric model with CESM (i.e., CAM5) have credibly represented cloud-sea ice feedbacks for the right reasons (Morrison et al., 2019), while others (i.e., CAM4) have not (Kay et al., 2011b). CESM version 2 (CESM2) has been publicly released and data from two configurations – CESM2(CAM6) and CESM2(WACCM6) (hereafter called CAM6 and WACCM6) – are freely available.

The purpose of this manuscript is to 1) document the Arctic and Antarctic sea ice in the two CESM2 configurations over the historical and preindustrial (PI) periods, and 2) investigate the source of differences in the sea ice state between these configurations. Many other aspects of the sea ice simulation in CESM2 and comparisons with previous versions of the model must be explored for fuller understanding but are beyond the scope of this paper, and relevant complementary sea ice studies will be referenced when appropriate. Section 2 describes the two CESM2 configurations used in this analysis and highlights the differences in simulations. We examine the PI and historical sea ice in the Arctic and Antarctic in section 3. In section 4, we focus on the Arctic and investigate the differences in PI sea ice surface energy budget, mass budget, and clouds. A discussion and conclusions are presented in section 5.

2. Data and Methods

2.1 The Community Earth System Model Version 2 (CESM2)

The CESM2 is a freely available, community-developed fully coupled earth system model. The model components are atmosphere, ocean, land, sea ice, and land ice models that exchange information through a flux coupler. The major new features and capabilities of CESM2 have been documented by Danabasoglu et al. (2020) and additional details about the CESM2 experiments contributed to the Coupled Model Intercomparison Project Phase 6 (CMIP6) can be found there as well. In this manuscript we will discuss in detail only the components relevant to the analysis presented.

Two versions of CESM2 were contributed to the CMIP6 archive (https://esgf-node.llnl.gov/projects/cmip6/) and differ only in their atmospheric configurations. As described by Danabasoglu et al. (2020), the CAM6 experiments use the Community

Atmosphere Model version 6 (CAM6) while the WACCM6 experiments use the Whole Atmosphere Community Climate Model version 6 (WACCM6; Gettelman et al., 2019). Both CESM2 configurations use nominal 1° (1.25° longitude x 0.9° latitude) horizontal resolution, the same finite volume dynamical core, and identical parameterization tuning. A major difference between the atmospheric models is that CAM6 has 32 vertical levels with the model top in the stratosphere at 3.6 hPa (~40 km) while WACCM6 has 70 vertical levels with a model top in the lower thermosphere at $6x10^{-6}$ hPa (~140 km). The vertical level spacing is identical between CAM6 and WACCM6 from the surface to 87 hPa. Another major difference is that WACCM6 has comprehensive chemistry with both prognostic chemical species and prognostic aerosols. Those include the formation of secondary organic aerosols (SOA) from precursor emissions using the volatility basic set (VBS) approach (Tilmes et al., 2019) and interactive stratospheric aerosols (Mills et al., 2017). On the other hand, CAM6 has limited chemistry and prescribes tropospheric and stratospheric oxidants that feed the aerosol model. As detailed by Danabasoglu et al. (2020), these oxidants in CAM6 were obtained from WACCM6 simulations in order to use consistent forcings in both CAM6 and WACCM6 simulations.

The sea ice and ocean models are identical in the CAM6 and WACCM6 configurations, and they share a horizontal grid. The horizontal resolution is a uniform 1.125° in the zonal direction. The resolution varies in the meridional direction: in the Arctic, the minimum resolution is approximately 0.38° in the northwestern Atlantic Ocean while in the northwestern Pacific Ocean the maximum resolution is about 0.64°, and in the Antarctic the resolution is constant at 0.53°. To represent sea ice, CESM2 uses the CICE model version 5.1.2 (Hunke et al., 2015). Both configurations of CESM2 have identical sea ice physics and parameters, and both use the new mushy-layer thermodynamics (Turner & Hunke, 2015; Bailey et al., 2020) as well as the level-ice melt pond parameterization (Hunke et al., 2013). In these experiments, CICE has five categories for the ice thickness distribution, and it uses eight vertical ice layers and three vertical snow layers to represent the vertical salinity and temperature profiles. CESM2 uses the modified Parallel Ocean Program version 2 (Smith et al., 2010; Danabasoglu et al., 2012) with updates as discussed by Danabasoglu et al. (2020). Both the CESM2 configurations use identical ocean physics.

The CAM6 and WACCM6 PI simulations were integrated for 1200 and 500 years, respectively. The shorter WACCM6 integration is due to the large increase in cost to run this model version and associated computational limitations. Over this period the global mean top of atmosphere heat imbalances were small at +0.05 and +0.06 W m^{-2}, respectively, and this gain is reflected only in the ocean component of the model (Danabasoglu et al., 2020). For the historical (1850-2014) period there are 11 CAM6 and three WACCM6 ensemble members. The historical CAM6 and WACCM6 experiments were branched from years in the respective PI experiments as detailed by Danabasoglu et al. (2020). Both the CAM6 PI and historical experiments used realistic chemical and aerosol constituents forcing derived from the WACCM PI control (for PI) and an average of the three historical WACCM6 experiments (for historical).

When analyzing the sea ice in historical experiments, we focus on the years 1979 to 2014 (36 years) in order to compare with the satellite observational record. Additionally, it is important to note that the CMIP6 "historical" experiments end in 2014, as per the CMIP protocol with regards to the forcing datasets. For the PI analysis we analyze the years 100-500 in each experiment. We omit the first 100 years of each simulation as the model was spinning up, and we analyze only overlapping years to minimize the likelihood that differences in the CAM6 and WACCM6 experiments are a result of the model drift from the much longer CAM6 PI. We use the variables output for the Sea Ice Model Intercomparison Project (SIMIP; Notz et al., 2016). Welch's t-test, which does not assume equal variance for the samples, was used to determine significance of differences in mean values; an F-test was used to determine significance between differences in variance.

2.2 Reference datasets for comparison

As noted above, the CMIP "historical" experiments end in 2014, so while observational data are available after 2014, for consistency purposes with the model experiments we will treat the historical period as 1979-2014 to overlap with the satellite observational record. Over the entire historical period, we compare the hemispheric average annual sea ice extent timeseries and annual cycle against the hemispheric sea ice index (Fetterer et al., 2017). The spatial locations of the observed ice edge are derived from the SSMR and SSM/I satellite data (Comiso, 2000). The sea ice edge is defined as cells with 15% concentration.

Unlike for sea ice extent, year-round, long-term gridded sea ice thickness and volume data over the Arctic and Antarctic Oceans are not available. We use five years of gridded ICESat satellite sea ice thickness data for the Arctic for the spring (FM; 2003-2007) and autumn (ON; 2004-2008) (Kwok et al., 2009). In addition, we use gridded seasonally averaged ICESat sea ice thickness data for the Antarctic for the summer (FM; 2003-2007) and spring (ON; 2004-2008) (Kurtz & Markus, 2012). It should be noted that the Antarctic sea ice thickness data is only available in areas with sea ice concentration of 50% and greater and that the data coverage is sparser over sea ice in the Antarctic as compared to the Arctic because of the satellite track coverage. In the Antarctic, as compared to the Arctic, there is additional uncertainty from snow loading on the sea ice.

In addition to these satellite observations, we also use reconstructed sea ice volume from the Pan-Arctic Ice-Ocean Modeling and Assimilation System (PIOMAS) and the Global Ice-Ocean Modeling and Assimilation System (GIOMAS) (Zhang & Rothrock, 2003). PIOMAS and GIOMAS sea ice volume data are not strictly observations. PIOMAS assimilates observed sea ice concentration and observed sea surface temperature, while GIOMAS assimilates only observed sea ice concentration. Both PIOMAS and GIOMAS are forced by the NCEP/NCAR atmospheric reanalysis (Kalnay et al., 1996). PIOMAS has been widely used as a reference dataset in the Arctic for sea ice volume and analysis, and has been found well to compare with available in situ observations (e.g. Schweiger et al., 2011; Laxon et al., 2013; J. Stroeve et al., 2014; Lindsay & Schweiger, 2015). However, GIOMAS has been less widely evaluated, in part because there are many fewer observations of Antarctic sea ice thickness against which evaluation is possible.

Additionally, it should be noted that atmospheric reanalysis products rely on data assimilation, and that data with which to assimilate are scarce in the Antarctic leading to additional uncertainty. While there is uncertainty with GIOMAS, we will use it as a reference in the Antarctic, as has been done in other climate model analyses (e.g., Shu et al., 2015), because it is the best available spatially and temporally extensive sea ice volume dataset in this region. Neither sea ice volume dataset should be considered "truth", but instead a consistent estimate of sea ice volume that is constrained by the atmospheric reanalysis.

We also compare modeled Arctic sea ice volume from 1984-2014 with a new satellite-derived product (Liu et al., 2020). The derived sea ice volume is based on the relationship between ice age and ice thickness from collocated observations and an empirical ice growth model. This relationship is then applied to derive sea ice thickness from the weekly satellite ice age product available since 1984 (Tschudi et al., 2019). The derived ice thickness and volume compare well with available satellite and submarine data, though they exhibit a stronger decreasing trend as compared to PIOMAS (Liu et al., 2020).

2.3 Northward Heat Transport calculations

Following Kay et al. (2012), we calculate the vertically integrated total northward heat transport (NHT, Watts). NHT into the polar regions results from a combination of atmospheric and ocean NHT, and sea ice export and the resulting latent heat loss from the ice melt:

$$NHT = NHT_{atm} + NHT_{ocn} + NHT_{ice} \qquad (1)$$

The total NHT across each latitude band (φ) and atmospheric NHT is calculated using monthly mean top of atmosphere (TOA) energy flux:

$$NHT = -2\pi {R_e}^2 \int_{\varphi}^{\pi/2} N \cos(\varphi)\, d\varphi \qquad (2)$$

where R_e is the radius of the earth in meters and N is the TOA energy flux (W m^{-2}, where positive indicates the earth gains energy). N is calculated using the monthly mean TOA net shortwave and longwave fluxes, which are standard model output. NHT_{atm} is then calculated:

$$NHT_{atm} = -2\pi {R_e}^2 \int_{\varphi}^{\pi/2} (N - n) \cos(\varphi)\, d\varphi \qquad (3)$$

where n is the total surface energy flux (W m^{-2}, positive when surface energy increases). n is calculated using the net shortwave and longwave surface fluxes and the turbulent sensible and latent heat fluxes, all of which are standard model output. We correct the latent heat flux to account for snow melt, as detailed in Kay et al. (2012). The vertically integrated NHT_{ocn} is calculated at each timestep during model integration and a standard model diagnostic output. NHT_{ice} is found as a residual. Further details regarding the NHT calculations are provided in the appendix of Kay et al. (2012). The NHT at a given latitude can be divided by the Earth's surface area north of that latitude to obtain an NHT forcing (W m^{-2}) that can be directly compared to other forcing (e.g. radiative forcing).

2.4 Sea ice energy and mass budget calculations

To better understand the processes driving sea ice evolution, we calculate the sea ice surface energy budget and mass budget. For these calculations, we use monthly mean variables output directly from the model simulations as part of the Sea Ice Model Intercomparison Project (SIMIP; Notz et al., 2016) subset of CMIP6. The SIMIP variable names are given in parenthesis, and further information about the SIMIP variables can be found in Notz et al. (2016).

The net surface energy flux (Q_{net}) at the sea ice-atmosphere interface can be written:

$$Q_{net} = \left(SW_{down} - SW_{up}\right) + \left(LW_{down} - LW_{up}\right) + Q_{sens} + Q_{lat} + Q_{cond} \quad (4)$$

where SW_{down} (siflswdtop) is the downward shortwave radiation, SW_{up} (siflswutop) is the upward shortwave radiation, LW_{down} (sifllwdtop) is the downward longwave radiation, LW_{up} (sifllwutop) is the upward longwave radiation, Q_{sens} (siflsenstop) is the net sensible heat flux, Q_{lat} (sifllatstop) is the net latent heat flux, and Q_{cond} (siflcondtop) is the net top conductive heat flux through the ice. All variables have units of W m^{-2} and positive values indicate surface energy gain.

The net change in sea ice mass (M_{net}) is given by:

$$M_{net} = M_{basal} + M_{frazil} + M_{snowice} + M_{top} + M_{bot} + M_{lat} + M_{evapsubl} + M_{dyn} \quad (5)$$

Ice mass gain occurs through ice growth at the base of existing ice (M_{basal}; sidmassgrowthbot), ice growth in supercooled open ocean water (M_{frazil}; sidmassgrowthwat), and transformation of snow to sea ice ($M_{snowice}$; sidmasssi). Ice mass loss occurs through melting at the top surface (M_{top}; sidmassmelttop), melting at the base of the ice (M_{bot}; sidmassmelttop), and melting on the sides of the ice (M_{lat}; sidmasslat); note all of these values are negative indicating ice loss. The ice can also gain or lose mass from evaporation or sublimation ($M_{evapsubl}$; sidmassevapsubl) or dynamical advection of ice into or out of the domain (M_{dyn}; sidmassdyn). These SIMIP mass budget variables all have units of kg m^{-2} s^{-1}, and a net positive (negative) value indicate ice mass gain (loss). The total mass budget terms, used in the budget above, are calculated as follows (using basal growth as the example term):

$$M_{basal} = \frac{\sum M_{basal\,(grid\ cell)} * area_{(grid\ cell)}}{\sum area_{(grid\ cell)}} \qquad (6)$$

Where we sum the mass change in each grid cell multiplied by the area of the grid cell over our region of interest, then normalize by the total area in the region. The result is the mean mass change, for each term, over the basin of interest per unit time. We have converted the change in mass to change in thickness (cm day^{-1}) using the constant sea ice density (917 kg m^{-3}) used by CICE within CESM2 as this quantity is easily comparable to observed sea ice mass change and is intuitive to visualize for an ice floe.

3. Sea Ice State

It is important to evaluate both the 2D areal coverage of sea ice, as measured by sea ice extent or concentration, in part because long term observational records exist of these fields and can be used as a reference. Yet, there is still high interannual variability of ice extent (Swart et al., 2015). It is also important to assess the 3D sea ice volume, which is defined as the mean grid cell thickness multiplied by the grid cell area. Hemispheric sea ice volume is less sensitive to internal variability and therefore more directly tied to climate forcing than 2D measures (e.g., Shu et al., 2015). Additionally, we examine the mean annual cycles to identify any systematic seasonal differences between CAM6 and WACCM6. Geographical locations or locations mentioned in the text are shown in Figure S1.

3.1 Arctic

In the Arctic, throughout the PI experiment the CAM6 sea ice extent is significantly lower than the WACCM6 extent (Figure 1a; Table 1). In the historical experiments, the ensemble mean extent for CAM6 is significantly lower than the WACCM6 ensemble mean for 23 of the 36 years in the historical period (Figure 1b). The observed Arctic sea ice extent falls within the WACCM6 ensemble spread, while the CAM6 ensemble spread tends to be lower than the observed sea ice extent. The model drifts slightly in the PI period, and both configurations lose a small amount of ice over time. The historical ensemble mean rate of loss is two orders of magnitude larger than in the PI period due to transient greenhouse gas forcing, and the 35-year trend in annual mean ice extent loss from both CESM experiments compares well with observations (Table 2). Further analysis about CESM2 ice extent trends in the historical period and for future scenarios is presented in detail in DeRepentigny et al., (2020) and thus not presented here.

The PI annual mean Arctic ice volume is significantly larger (by 3.9×10^3 km^3 during years 100-500) for WACCM6 than CAM6 (Figure 1c; Table 1). This difference is evident in the ensemble mean over the historical period, with CAM6 always being lower than WACCM6 by as much as $8x10^3$ km^3 (Figure 1d). The reconstructed mean sea ice volume from the WACCM6 ensembles is more similar to the PIOMAS and GIOMAS reconstructions, particularly later in the historical period (Figure 1d). Additionally, in the Central Arctic (see Figure 1e) the WACCM6 ice volume compares well throughout the historical period against newly available satellite derived ice volume data (Figure 1e). In sum, throughout the historical period the CAM6 sea ice volume is well below any reference dataset, while WACCM6 is more similar in magnitude. The historical rate of ice volume loss is lower in CAM6 than WACCM6, and the CAM6 rate is more similar with the reference data loss rates (Table 2). While the mean ice extent is smaller in CAM6 than WACCM6, as detailed above, the large differences in ice volume indicate that there must be large ice thickness differences between the CESM2 configurations as well and this will be explored later in this section.

Throughout the year, in both the PI and historical periods, the CAM6 hemispheric extent is significantly lower than WACCM6, though the difference is smallest in winter months (Figure 2a). In the historical period the maximum modeled ice extent occurs in March. The winter ice extent is lower than observed in both CESM2 configurations, mainly due to less ice coverage in the Pacific, including the Bering Sea and Sea of Okhotsk (Figure 3a). In both the PI and historical periods, the CAM6 experiments have less extensive winter ice than WACCM6, which is due to less ice coverage on both the Atlantic and Pacific margins of the sea ice pack with the largest differences occurring in the Atlantic sector (Figure 3c; Figure S2). The rate of spring ice loss for CAM6 is similar to observations until July, while the WACCM6 loss is slower than observed (Figure 2a).

Both CESM configurations reach the minimum ice extent in September. The CAM6 mean September extent is significantly lower than WACCM6 in both the PI and historical periods by $1x10^6$ km^2 and $2x10^6$ km^2 respectively, and much lower than observed (Figure 2a). The WACCM6 ensemble mean summer extent is similar to observations in the hemispheric average and spatial coverage of sea ice (Figure 2a, 3b). In contrast, the historical CAM6 summer sea ice extent is too low over much of the Arctic Basin with the largest difference in the East Siberian Sea (Figure 3d). A similar difference in ice concentration focused in the East Siberian Sea exists in the PI period between CAM6 and WACCM6 (Figure S2).

In every month, in both the PI and historical periods, the CAM6 sea ice volume is significantly lower than the WACCM6 sea ice volume (Figure 2c). While the WACCM6 monthly mean ice volume is more similar to the PIOMAS and GIOMAS products, the timing of the WACCM6 ice volume loss is delayed by a month compared to the reconstructed volume and remains a bit higher during the annual September minimum.

We use the standard deviation to quantify monthly variability of sea ice extent and volume. In both time periods the summer ice extent variability is higher than the winter variability (Figure 2b) because the winter ice extent is constrained primarily by the land boundaries and ocean heat content (Bitz et al., 2005). There is greater ice extent variability throughout the year in the historical period compared to the PI likely due to thinner sea ice (Goosse et al., 2009; Holland et al., 2008), and this increase is particularly large in summer months. The CAM6 historical summer ice extent variability is much higher than WACCM6, which is likely due to differences in the ice thickness detailed later in this section. In the historical period, the year-round CAM6 ice volume variability is similar magnitude to the PIOMAS and GIOMAS variability, and it is significantly lower than WACCM6 (Figure 2d).

In the Central Arctic, the WACCM6 ensemble mean has a higher fraction of thicker ice than CAM6 in both spring and autumn (Figure 4). The ICESat observations (available 2003-2009) and WACCM6 have similar peaks for most likely ice thicknesses, but the ICESat observations have higher fractions of very thick ice in both seasons (Figure 4). While the modeled ice is thinner than observed across the entire Central Arctic in both seasons, the largest differences with ICESat occur along the Canadian Arctic Archipelago and are co-located with the thickest sea ice (Figure 5). When we examine a longer historical period and the PI records, neither of which have observations against which we can compare, we find that the ice thickness distributions for CAM6 and WACCM6 remain distinctly different. In each time period, CAM6 has a lower fraction of thicker ice in both winter and summer (Figure S3), and the largest magnitude spatial thickness differences occur in the East Siberian Sea region (Figure S4,S5).

3.2 Antarctic

In the Antarctic, we find that CAM6 and WACCM6 mean extents are not statistically different for PI years 100-500 (Table 1; Figure 6a). The differences in between WACCM6 and CAM6 in mean sea ice extent (for years 100-500) are small, and the smaller CAM6 extent over years 100-1200 are attributable to the PI drift over the additional 700 years (Table 2). For the historical period, the two CESM configurations generally maintain similar sea ice extent: there are significant differences in the annual mean extent in only six of the 36 years over the historical period (Figure 6b). The net 35-year trend over the historical period has been observed to be positive, while all ensemble members from both configurations have a net negative trend over these years (Table 2). The modeled historical ice loss rate is two orders of magnitude larger than the PI rate, indicating that differences in forcing rather than model drift are likely to drive the historical trends. The discrepancy in the sign of modeled and observed trends in Antarctic sea ice has been previously documented for climate models (e.g. Landrum et al., 2012; Mahlstein et al., 2013; J. Turner et al., 2013; Hobbs et al., 2015; Shu et al., 2015). The observed dramatic loss after 2014 in Antarctic sea ice (Stuecker et al., 2017; Meehl et al., 2019; Wang et al., 2019; Parkinson, 2019) occur after the CMIP6 historical forcing period, which ends in December 2014, and are still being investigated. For mean ice volume, over the PI the volume is similar with CAM6 slightly lower than WACCM6 over years 100-500 (Table 1; Figure 6c). During the historical period there are only four years in which the ensemble mean volume is significantly different between CESM2 configurations (Figure 6d), and both the CESM2 configurations have a negative ice volume trend while GIOMAS trends are positive (Table 2).

The mean annual cycle of Antarctic sea ice extent in the PI and historical periods is similar for both the CAM6 and WACCM6 experiments (Figure 7a). While the timing and magnitude of the historical minimum February sea ice extent agree well with NSIDC observations, the maximum extent occurs in October and is ~$2x10^6 km^2$ smaller than the observed maximum in September. There is no significant difference in monthly mean ice extent variability in the PI between the CAM6 and WACCM6 experiments, though there is in the historical. Spatially, the WACCM6 maximum ice concentration is too low in the Indian Ocean sector of the Antarctic basin (Figure 8b). While the ice concentration differences between CAM6 and WACCM6 are heterogenous and mostly insignificant (Figure 8c,d), in winter months CAM6 has lower extent in the Atlantic and Indian Ocean sectors compared with WACCM6 (Figure 8). In the PI period, however, CAM6 has slightly higher ice concentration in the wintertime Indian and Pacific Ocean sectors (Figure S6). There are differences in the timing of the minimum or maximum volume between the two configurations and GIOMAS, with the largest magnitude differences during wintertime (Figure 7c). However, as mentioned previously, there are uncertainties associated with GIOMAS volume due to poorly constrained atmospheric reanalysis in these regions.

While there are uncertainties in satellite observations of ice thickness, we compare the spatial ice thickness in both CESM2 configurations with ICESat for 2003-2009. Overall both CESM2 configurations have thicker ice than observed around the continent, but the CESM2 ice is particularly thick in the Amundsen Bellingshausen Seas (Figure 9). Spatially, the differences between CESM2 experiments in PI and historical thickness are mostly small, insignificant, and heterogeneous, and the largest thickness differences are found at the ice edge or in the Weddell Sea (Figure S7,S8). Histograms indicate that in both the historical and PI the winter ice thickness distributions are similar in CAM6 and

WACCM6, and there are slight differences in summer historical distributions (Figure S3).

A full examination of the WACCM6 and CAM6 sea ice mass and energy budgets (Figure S9) shows that there are not significant differences in the net budgets in the Antarctic between configurations. This is consistent with the very similar mean sea ice state. Because the mean states are so similar between the CAM6 and WACCM6 configurations, we will not discuss the Antarctic further in this paper. Please refer to (Raphael et al., 2020; Singh et al., 2020) for further analysis of the Antarctic sea ice in CESM2 with the CAM6 atmospheric component.

4. Exploring Differences in Preindustrial Arctic Sea Ice

The differences in the mean Arctic sea ice extent and volume are surprising given that the two CESM2 configurations have small atmospheric differences – primarily in the model top and in the treatment of atmospheric chemistry. We examine the forcing and processes that govern ice growth and melt to better understand these mean state differences. Many of the differences between CAM6 and WACCM6 exist in both the historical and PI periods, but the following analysis corresponds to PI years 100-500 for both CAM6 and WACCM6 because there are many years for analysis without the additional influence of transient atmospheric forcing. We focus on the region north of 70°N since it has the largest differences in ice thickness and extent (Figure S1; Figure S5).

4.1 Northward Heat Transport

We use NHT to identify whether differences in heat flux convergence between CESM2 configurations could account for the differences in Arctic sea ice mean state. Equations detailing the calculations shown in this paper are presented in section 2.3. We find that in both the CAM6 and WACCM6 configurations the atmospheric component of the NHT dominates the total NHT, which peaks at about 6 PW, while the sea ice component is the smallest (Figure S10a). The net differences between the configurations are small (less than 2% the total NHT) and primarily due to atmospheric NHT (Figure S10b). When we examine the NHT differences as a forcing we find that over the Arctic CAM6 has 2-4 W m^{-2} less NHT than WACCM6 (Figure 10a). This suggests that, given NHT alone, CAM6 might be expected to have more extensive and thicker ice, which is the opposite to our results and implies another cause for the differences in CESM2 configurations. Additionally, there are not significant differences in global or Northern Hemisphere surface temperature climate between CESM2 configurations during the overlapping simulation years (Table 1). We also find statistically insignificant differences in mean sea level pressure and surface winds in the Arctic (not shown), which suggests atmospheric circulation differences that could impact the sea ice dynamics and drive differences in thickness are not responsible.

4.2 Mass and Energy Budgets

We examine the annual cycle of the sea ice mass budget to determine causes driving the differences in ice growth and melt. There is net growth from September to May, mainly due to congelation sea ice growth at the bottom of the ice (Figure S6c). During the growth season, CAM6 has more ice growth, due primarily to congelation ice, than WACCM6 (Figure 10b). The increased ice growth for the CAM6 configuration is likely due to the thinner ice, which is less insulating, allowing for increased heat conduction through the sea ice (Maykut, 1982). Both configurations have net ice mass loss from May through September that is dominated by bottom melt (Figure S10c). Increased summertime bottom melt in CAM6 dominates the net mass budget differences (Figure 10b; Figure S10c).

To investigate differences in the sea ice mass budget, we also examine differences in the annual surface energy budget north of 70°N. We examine both the surface energy budget for sea ice alone as well as the combined ice and ocean surfaces. The ice surface loses heat from September to May (Figure 10c), which corresponds to the period of net ice mass gain (Figure 10b). In the autumn (October-November) the CAM6 ice surface loses ~7 W m^{-2} more than in WACCM6 (Figure 10c), which corresponds to the increase in congelation growth at this time (Figure 10b). From June to August both the CAM6 ice surface and total ice plus ocean surface gain a maximum of ~4 W m^{-2} more than the WACCM6 surface (Figure 10c). The largest drivers of the difference in the surface energy budgets are the downward shortwave and longwave radiative components (Figure 10c). In particular, CAM6 has over 10 W m^{-2} more incoming shortwave radiation, which is partly compensated by ~6 W m^{-2} less incoming longwave radiation to both surfaces compared to WACCM6. The incoming radiative differences are largest in June, but they persist through the melt season. As expected with near-freezing surface temperatures throughout the melt season, the outgoing longwave radiation is similar between the configurations during the melt season. The outgoing shortwave radiation is slightly higher in CAM6, and further analysis, detailed below, will determine if this difference is due to more incoming shortwave or an increase in albedo.

Changes in surface albedo over sea ice are due to changes in ice surface conditions (e.g. the loss of snow cover coupled with the increase in melt pond coverage), while the differences in the total surface albedo are due to the combination of ice surface changes and changes in ice fraction. CAM6 has a lower ice albedo and total surface albedo than WACCM6, and the differences from WACCM6 are largest in August (Figure 11a). The divergence between the ice albedo and surface albedo differences indicates that changes in ice fraction between CAM6 and WACCM6 become increasingly important later in the melt season. The seasonal progression through the melt season is important for driving these changes.

The changes to the surface albedo and the resulting albedo feedback are likely responsible for the mismatch in timing of maximum shortwave radiation differences (June) and the maximum melt differences (July). In May and June, the sea ice is covered by snow and the ice fraction is relatively similar between CAM6 and WACCM6 (Figure 11b). Additional incoming solar energy in CAM6 results primarily in increased surface snow melt and not top melt of the ice itself (Figure 10b; Figure 11c). As a result of earlier surface snow melt, the ice albedo in CAM6 decreases due to both the combination of bare ice and melt pond coverage. The change in ice surface albedo results in increased solar absorption, increased ice top melt, and a sharper decrease in sea ice fraction. As a result of the decrease in ice coverage, the ocean absorbs solar radiation. This ocean energy gain drives large differences in bottom melt by July, melting more ice.

The differences in NHT indicate that the CAM6 experiments have less heat flux convergence from lower latitudes into the Arctic as compared to WACCM6. This cannot explain the thinner ice present in the CAM6 simulations. Instead, the differences in mean ice state between CAM6 and WACCM6 are related to local differences in radiation. The difference in radiation triggers the ice-albedo feedback earlier in the CAM6, and this feedback amplifies the differences in ice state later in the melt season when the radiative differences are smaller. It is important to understand how the atmosphere in these CESM2 configurations directly lead to the large differences in surface radiative fluxes.

4.3 *Clouds*

Based on the differences in radiative fluxes, which are closely related to clouds, we examine differences in the Arctic shortwave feedbacks north of 70°N to investigate their impact on the difference in mean sea ice state in the CESM2 configurations. Of particular interest are: 1) the positive shortwave surface feedback in which melting ice and snow lower surface albedo, increasing surface shortwave absorption; and 2) shortwave cloud feedbacks, including the negative shortwave cloud feedback that results from increases in liquid water resulting in higher cloud albedo and decreasing surface shortwave absorption (Goosse et al., 2018). We evaluate these feedbacks using the approximate partial radiative perturbation (APRP) method (Taylor et al., 2007). During the summer melt season, we find that the combination of the surface albedo and cloud shortwave feedbacks lead to greater shortwave fluxes in CAM6 than WACCM6, and that the magnitude of the cloud term differences is larger than the surface term (Figure 12a). CAM6 has a larger positive surface albedo feedback, consistent with the differences in surface albedo discussed previously. For a negative cloud feedback, the positive difference indicates that CAM6 has a smaller cloud feedback than WACCM6.

We examine differences in the Arctic cloud properties north of 70°N to identify how the clouds differ throughout the year in CAM6 and WACCM6. The liquid water path (LWP) is defined as the sum of the total liquid water in the atmospheric column, and similarly the ice water path (IWP) is defined as the sum of the total ice water in the atmospheric column. Compared to WACCM6, CAM6 has both lower LWP and IWP through the summer months (Figure 12b). In May, CAM6 has ~22% lower LWP than WACCM6, and in June CAM6 has ~25% less IWP. Throughout the year both configurations have cloud fractions above 80% and the difference in cloud fraction between the two configurations is never greater than 4% (Figure 12b). Maps of cloud property differences show large and significant differences in LWP all summer that are co-located with the sea ice (Figure 13). In contrast, the absolute differences in IWP and cloud fraction are more consistent over both land and ocean (Figure 13), though maps show that the largest percent differences occur over the Arctic sea ice throughout the melt season (Figure S11).

As described in Section 2, the CESM2 configurations that use CAM6 and WACCM6 have identical sea ice parameters and atmospheric cloud parameters. One important way they differ, however, is with the inclusion of comprehensive chemistry and prognostic aerosols including an improved formation of secondary organic aerosol (SOA) within the WACCM6 (see Tilmes et al., 2019). During spring there are fewer accumulation mode SOA, primary organic matter, black carbon, and sulfate aerosols over sea ice in CAM6 as compared to WACCM6 (Figure 14). These differences in aerosol are similar in summer for all aerosols except the SOA. In addition to fewer aerosols, there are also fewer liquid cloud condensation nuclei (CCN) and cloud droplets in CAM6 (not shown). Thus, in WACCM6 the improved aerosol formation in source regions outside the Arctic causes an increase in the aerosols in the accumulation mode (in CESM2: 0.06-0.5 μm - the size most relevant for CCN as they accumulate in the atmosphere and can be transported) and therefore the amount of CCN reaching the Arctic. In the WACCM6 configuration, more Arctic CCN tend to result in more and smaller cloud drops. As a result, there is less precipitation, a longer lifetime for cloud drops, and higher LWP and cloud fractions, which results in reduced shortwave flux to the surface that is only partially compensated by increased longwave flux to the surface.

5 Discussion and Conclusions

We present the Arctic and Antarctic sea ice mean state from available PI and historical experiments from two configurations of the CESM2 submitted to CMIP6. In the Arctic, there is a significant difference in sea ice extent and thickness in both the PI and historical periods between the CAM6 and WACCM6 configurations, with WACCM6 having thicker and more extensive ice. In the historical period, both CESM2 configurations well capture the decreasing trends in ice extent and ice volume observed over the historical period as well as timing of the seasonal cycle in ice extent and volume.

In the winter, both configurations underestimate the maximum ice extent, but in summer the WACCM6 minimum sea ice extent is very similar to observed while the CAM6 sea ice extent is significantly lower. In both the PI and historical periods, the WACCM6 sea ice is significantly thicker over the Arctic Basin throughout the year as compared to CAM6. While the WACCM6 ice thickness is closer to observations, the model still fails to capture the very thick ice observed along the Canadian Archipelago. There are significant differences in the extent and volume variability between configurations as a result of the sea ice thickness differences between the configurations. Further analysis should be done to better understand trends and variability in the PI period as compared to a similar length of time as the historical period.

In the Antarctic, the CAM6 and WACCM6 configurations are very similar in ice extent and thickness throughout the year. While both CESM2 configurations have sea ice extents similar to those observed, all ensembles have a decreasing trend in ice extent, contrary to observations. Additionally, both CESM2 configurations capture the Antarctic minimum extent but tend to underestimate the maximum extent and it occurs one month after the observed maximum. In contrast to the Arctic, the CAM6 and WACCM6 sea ice thickness in the Antarctic is not significantly different in the historical or PI period. This is consistent with the mechanism suggested about for the Northern Hemisphere: there would not be additional cloud condensation nuclei (CCN) over the Southern Ocean region since the major sources of sea salt and dimethyl sulfide (DMS) as CCN are present in both CAM6 and WACCM6.

The seasonality of the cloud differences between CESM2 configurations is especially important for the sea ice response due to the impacts on the albedo feedback. A detailed analysis of the CESM2 Arctic clouds has been completed by McIlhattan et al., (2020), and we focus on only the cloud differences in CAM6 and WACCM6 that drive differences in sea ice state. Previous observational and modeling studies have shown that from approximately May/June through September the clouds and sea ice decouple due to the relatively high static stability and low air-sea temperature gradients, so during these months cloud forcing impacts sea ice evolution but sea ice does not strongly drive cloud evolution (Kay & Gettelman, 2009; Morrison et al., 2018; Morrison et al., 2019; Huang et al., 2019). While there are not shortwave radiative impacts during polar night, longwave radiative impacts from clouds can still affect the surface. However, during winter months, when there is active coupling between the clouds and sea-ice, the differences in clouds between CAM6 and WACCM6 are small and contribute little to differences in the sea ice mass budget. Near-surface liquid-water clouds are known to dominate cloud radiative impacts in the Arctic (Morrison et al., 2018; Shupe & Intrieri, 2004). In early spring the sea ice in CAM6 experiences up to 16 Wm $^{-2}$ more incoming shortwave radiation (and up to 8 Wm $^{-2}$ less incoming longwave radiation) than in WACCM6. The modeled cloud fraction is fairly similar between experiments, but through the melt season there is significantly more liquid water in the WACCM6 clouds than in CAM6 indicating thicker cloud cover. The differences in incoming radiation and liquid cloud are largest in early spring (May/June) when there is not yet a large difference in sea ice fraction and near the transition period where the clouds become uncoupled from the sea ice below. While there are differences in the cloud shortwave forcing throughout the melt season, it is the impact of the early springtime forcing that initiate differences in snow and ice melt, which sets off an albedo feedback. Similar mechanisms in timing of cloud radiative fluxes have been found to affect the sea ice extent and volume biases in other coupled models (e.g. West et al., 2019). As the thinner ice in the CAM6 configuration melts slightly earlier, the area of ocean covered by sea ice decreases and dark ocean water is exposed, leading to increased absorption of incoming shortwave radiation that in turn heats the ocean waters and increases the ability to melt sea ice from below exposing more ocean (Perovich et al., 2007). Ultimately this leads to less summer ice cover in CAM6, less ice persisting through the year, and a thinner mean sea ice pack throughout the Arctic Basin. The spatial differences in liquid water path (LWP) during the melt season are centered over sea ice covered regions while the ice water path (IWP) difference is more hemispherically uniform. The clouds and sea ice are decoupled in these months; therefore, the processes constraining the large differences in LWP to be over sea ice would not be driven by surface fluxes, and further in-situ observations of the coupling between clouds, aerosols, and sea ice could better identify possible mechanisms.

The two CESM2 configurations analyzed share identical atmospheric dynamical cores, identical resolution for the atmosphere, ocean, and sea ice, and identical parameterization tuning for these same components. Additionally, the WACCM6 experiments provide the forcing for CAM6 experiments. The fundamental difference in the CESM2 configurations driving differences in the Arctic clouds is the inclusion of interactive chemistry and prognostic aerosols in WACCM6. Similar differences in aerosols and cloud forcings were found in WACCM6 experiments with a simplified secondary organic aerosol (SOA) parameterization as used in CAM6 (Tilmes et al., 2019). Of particular importance are differences in the formation of SOA over source regions as the result of the comprehensive SOA parameterization in WACCM6. This results in changes in particulate organic matter, black carbon, and sulfate aerosol reaching high northern latitudes through long-range transport. Because the relative aerosol differences exist in both the PI and present-day conditions, the differences in CCN production between CAM6 and WACCM6 do not depend strongly on transient greenhouse gas forcing. Differences in the Arctic sea ice state between CAM6 and WACCM6 in the historical and future scenario experiments may show similar mean state differences as shown here, but this will likely depend on the evolution of aerosol emissions impacting the Arctic clouds. In the WACCM6 configuration more aerosols are transported to the Arctic that are available as CCN for cloud droplet formation. In the Antarctic, there is not a significant difference in the mean sea ice state or mass budgets, which may be because there is not a difference in aerosol transport to the region. Future work should analyze the transport mechanisms and pathways of these aerosols to determine possible extra-polar source regions that may be impacting Arctic clouds, which then in turn force the sea ice below. Credibly simulating polar cloud processes, including understanding the aerosol transport into the polar regions, is essential for realistic and believable historical and future climate projections of sea ice cover in both poles.

6 Model and Data Availability

Previous and current CESM versions are freely available (www.cesm.ucar.edu:/models/cesm2). The CESM2 data analyzed in this manuscript have been contributed to CMIP6 and are freely available at the Earth System Grid Federation (ESGF; https://esgf-node.llnl.gov/search/cmip6/), from the NCAR Digital Asset Services Hub (DASH; https://data.ucar.edu), or from the links provided from the CESM website (www.cesm.ucar.edu). The scripts used for this analysis in this paper can be found at: https://github.com/duvivier/CESM2_sea_ice_JGR_2019

7 Acknowledgements

The CESM project is supported primarily by the National Science Foundation (NSF). This material is based upon work supported by the National Center for Atmospheric Research (NCAR), which is a major facility sponsored by the NSF under Cooperative Agreement No.1852977. Computing and data storage resources, including the Cheyenne supercomputer (doi:10.5065/D6RX99HX), were provided by the Computational and Information Systems Laboratory (CISL) at NCAR. We thank all the scientists, software engineers, and administrators who contributed to the development of CESM2. J. E. Kay was supported by NSF CAREER (AGS #1554659). M. M. Holland acknowledges support from NSF #1724748.

Figures and Tables

		CAM6 (yrs. 100-1200)		CAM6 (yrs. 100-500)		WACCM6 (yrs. 100-500)	
		mean	standard deviation	mean	standard deviation	mean	standard deviation
Surface Temperature (K)	Global	**278.3**	**1.6**	278.2	1.6	278.1	1.7
	NH	**257.5**	**11.7**	257.3	11.8	257.3	12.0
	SH	**252.6**	**6.5**	252.5	6.5	252.4	6.5
Sea Ice Extent (10^6 km^2)	NH	**12.0**	**0.30**	**12.1**	0.30	12.3	0.27
	SH	**13.1**	**0.48**	13.6	0.46	13.5	0.44
Sea Ice Volume (10^3 km^3)	NH	**22.3**	1.96	**23.1**	1.96	27.0	1.93
	SH	**14.1**	0.91	**14.5**	0.89	14.2	0.84

Table 1: CAM6 and WACCM6 global, Northern Hemisphere (NH), and Southern Hemisphere (SH) annual mean and standard deviation surface temperature (K), sea ice extent (10^6 km^2), and sea ice volume (10^3 km^3). Means were calculated from the PI experiment over the years listed. Bold values in the CAM6 columns indicate when the value is significantly different at the 95% level from WACCM6 as as determined by a Welch's t-test for the mean values and an F-test for the standard deviation values.

		Preindustrial		Historical (1979-2014)		
		CAM6 (yrs. 100-1200)	WACCM6 (yrs. 100-500)	CAM6	WACCM6	Reference
Sea Ice Extent (10^6 km^2/decade)	NH	-0.0031	-0.0063	-0.53	-0.52	-0.53
	SH	-0.0067	-0.011	-0.41	-0.56	+0.20
Sea Ice Volume (10^3 km^3/decade)	NH	-0.020	-0.031	-2.72	-4.82	-2.50 (-3.03)
	SH	-0.013	-0.015	-0.68	-0.86	+0.55

Table 2: Hemispheric trends in annual mean sea ice extent (10^6 km^2/decade) and sea ice volume (10^3 km^3/decade) for CAM6 and WACCM6 ensemble mean during the PI and, in parenthesis, historical periods. The observed historical trend in sea ice extent is calculated from the NSIDC sea ice index (Fetterer et al., 2017). The observed historical trend in sea ice volume is from the reference GIOMAS dataset (Zhang and Rothrock, 2003), and for the Northern Hemisphere the PIOMAS sea ice volume trend (Schweiger et al., 2011) is shown in parenthesis.

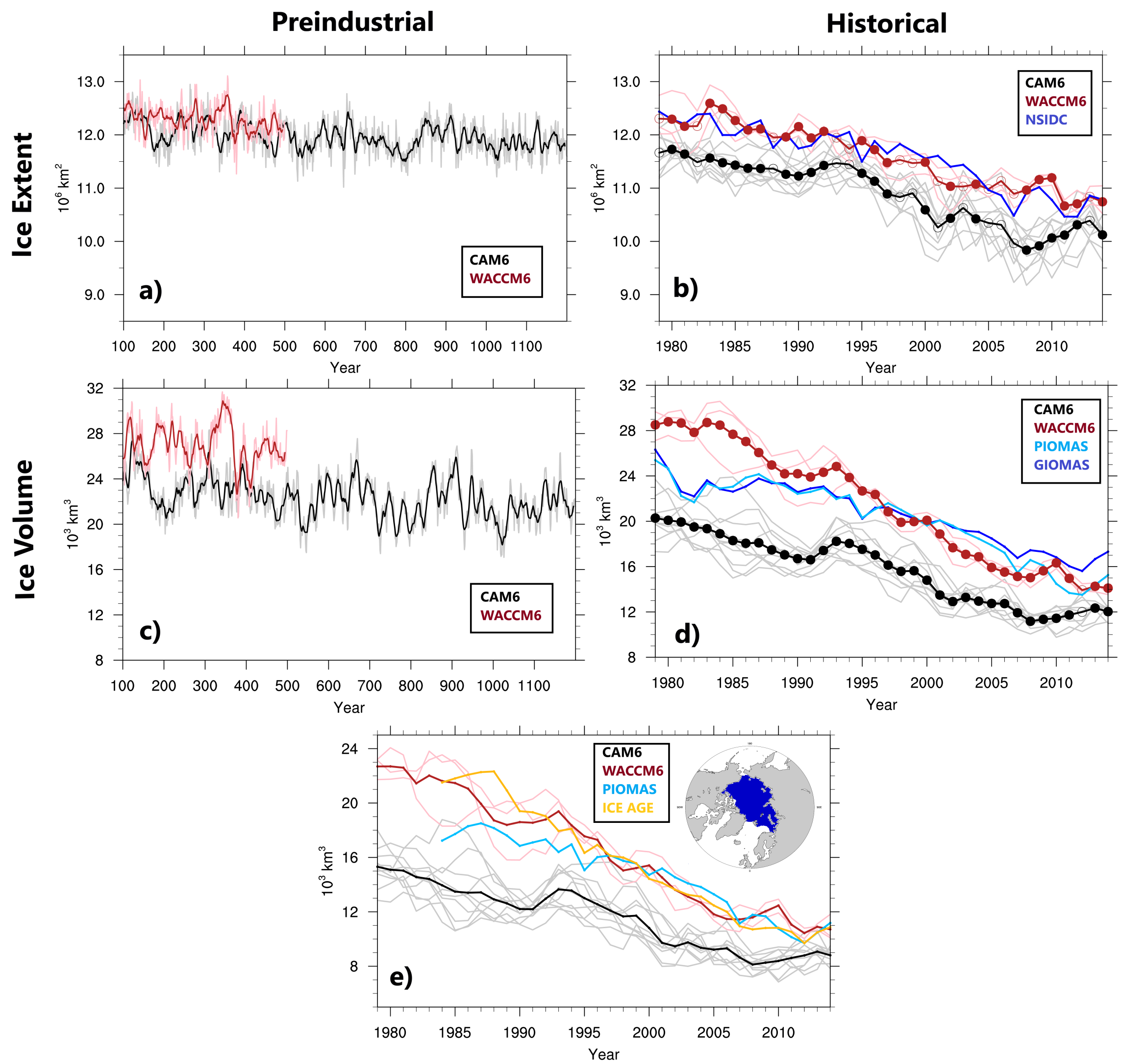

Figure 1: Time series of the (a), (b) annual mean Northern Hemispheric sea ice extent (10^6 km^2) and (c), (d) annual mean Northern Hemispheric sea ice volume (10^3 km^3), and (e) Arctic Basin (inset) annual mean sea ice volume (10^3 km^3). In (a),(c), for the PI period the 10-year running mean and raw annual values are shown for CAM6 (black and grey, respectively) and WACCM6 (red and pink, respectively). In (b),(d),(e) for the historical (1979-2014) individual ensembles and ensemble mean are shown for CAM6 (grey and black, respectively) and WACCM6 (pink and red, respectively), and large solid circles indicate years in which the CAM6 and WACCM6 ensemble means are different at the

95% significance level. In (b) the NSIDC sea ice index (Fetterer et al., 2017) is shown in blue. In (d) the reference sea ice volume for PIOMAS (Schweiger et al., 2011) and GIOMAS (Zhang and Rothrock, 2003) are shown in light blue and dark blue respectively, and (e) includes both the PIOMAS reference sea ice volume and the Ice Age ice volume (Liu et al. 2019) in orange.

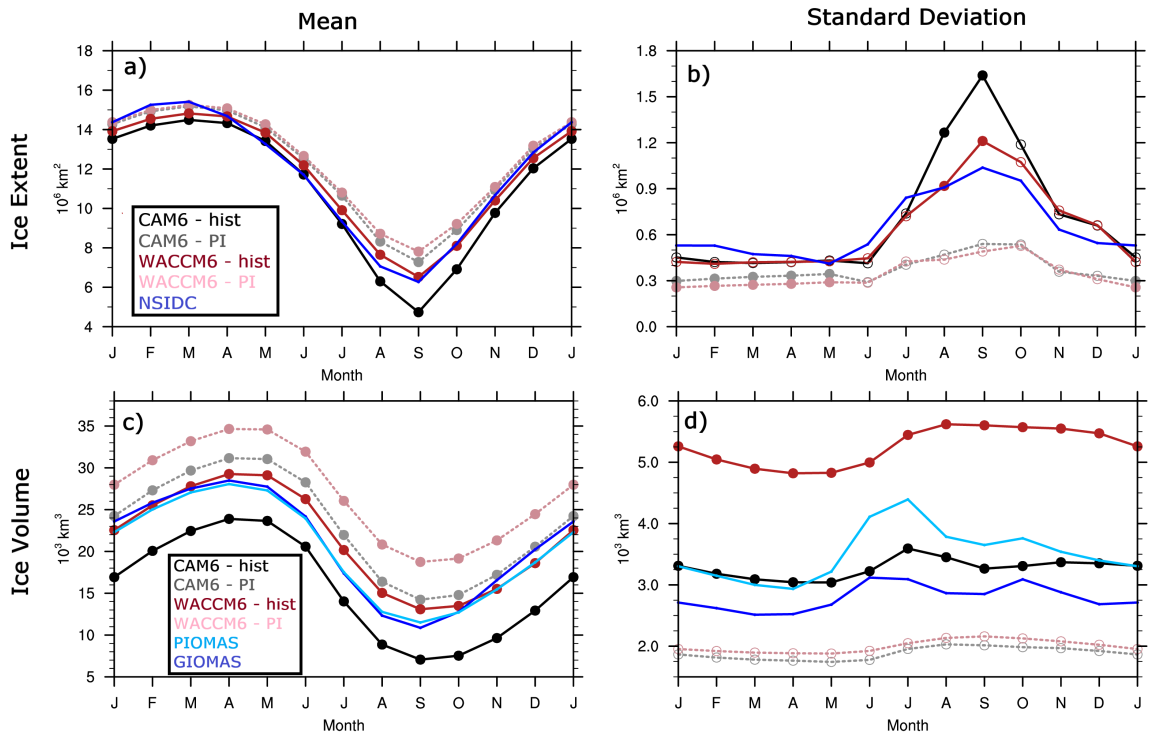

Figure 2: Northern Hemispheric annual cycle of (a), (b) sea ice extent (10^6 km^2) and (c), (d) sea ice volume (10^3 km^3) for the (a),(c) mean and (b),(d) standard deviation. The PI statistics are calculated over years 100-500, and historical statistics are calculated for 1979-2014 and all ensemble members. Large solid circles indicate months in which the CAM6 and WACCM6 ensemble means are different at the 95% significance level. In (b),(c) the NSIDC sea ice index (Fetterer et al., 2017) is shown in blue. In (c),(d) the reference sea ice volume for PIOMAS (Schweiger et al., 2011) and GIOMAS (Zhang and Rothrock, 2003) are shown in light blue and dark blue respectively.

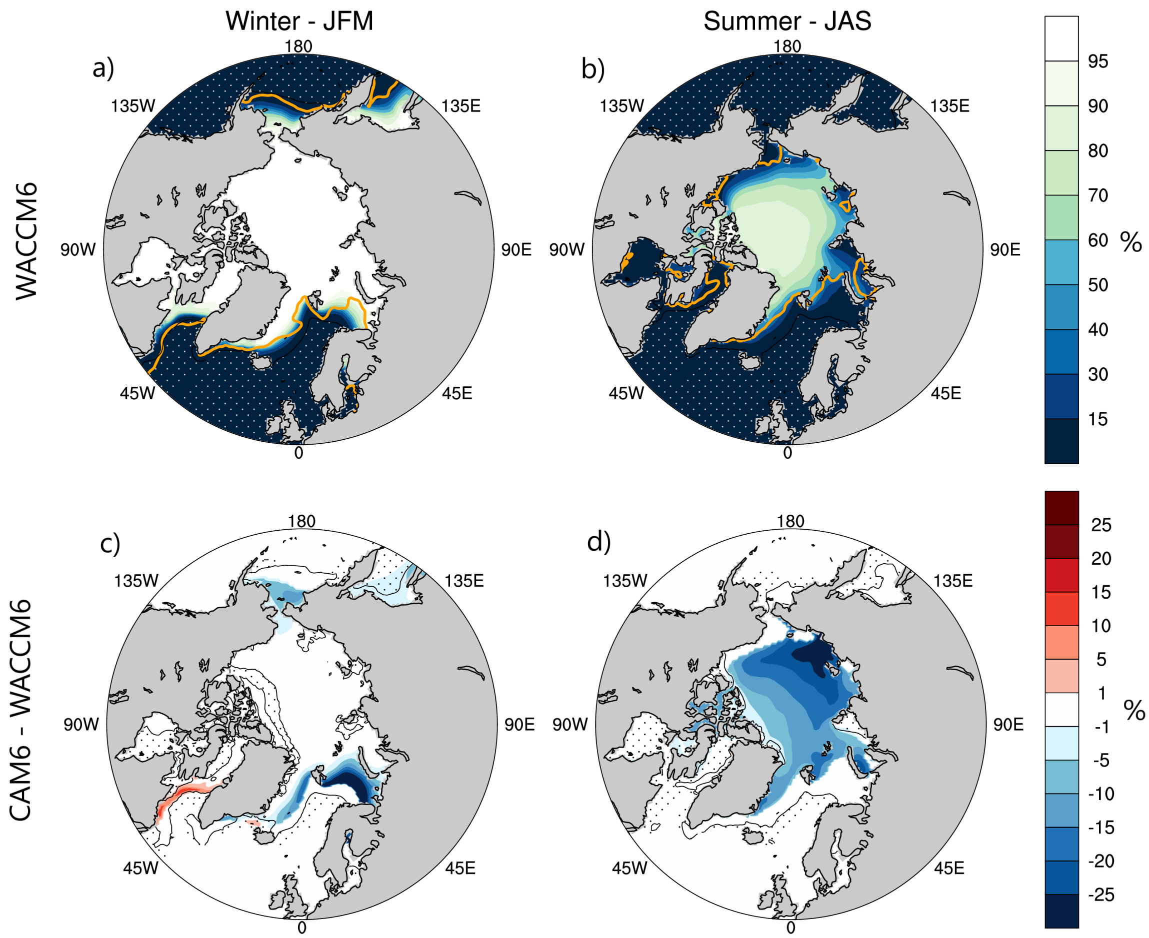

Figure 3: Arctic historical (1979-2014) ensemble mean sea ice concentration (%) for (a),(b) WACCM6 and (c),(d) difference (CAM6-WACCM6) in winter (January-March) and summer (July-September) months. In (a),(b) stippling indicates grid points where WACCM6 has 0% sea ice concentration, and in (c),(d) stippling indicates locations where the CAM6 and WACCM6 values are not different at the 95% significance level. The observed sea ice edge (Comiso, 2000; concentration = 15%) is shown in orange on (a) and (b).

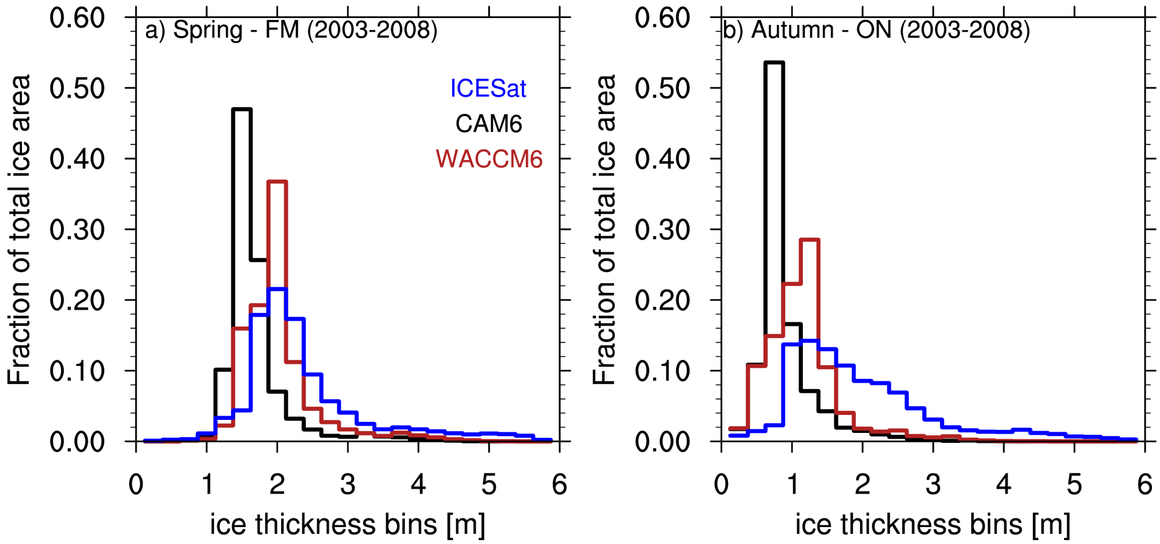

Figure 4: Histogram of the sea ice thickness (m) distribution in the Arctic Ocean for (a) spring (February-March) and (b) autumn (October-November) normalized by the fraction of the total ice area covered. The ICESat data (Kwok et al. 2009; blue) are averaged over autumn 2004-2008 and spring 2003-2007, while the CAM6 (black) and WACCM6 (red) data are averaged over 2003-2008 for both spring and autumn and only over the central Arctic Ocean where ICESat data are co-located (See Figure 5).

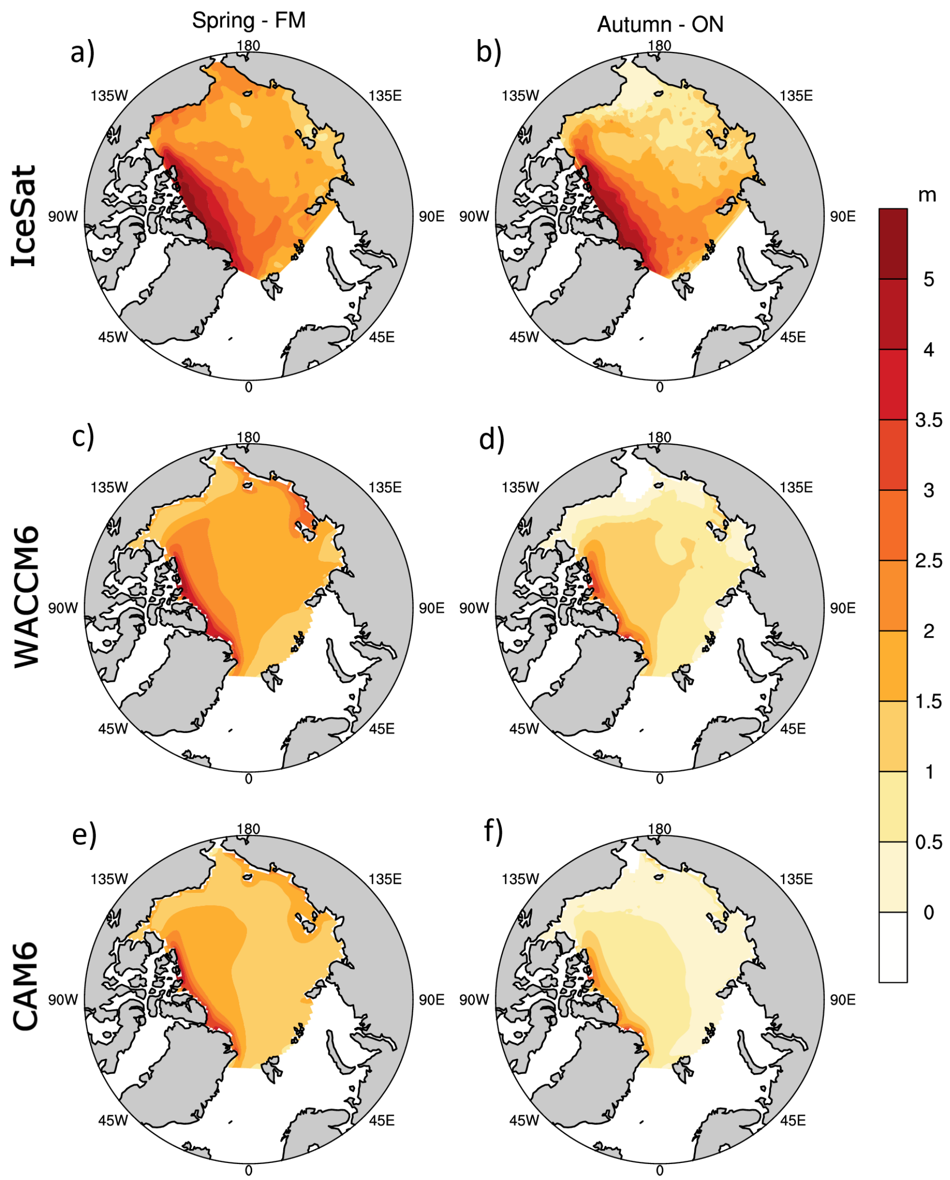

Figure 5: Sea ice thickness (m) from (a),(b) ICESat data (Kwok et al. 2009), (c),(d) WACCM6, and (e),(f) CAM6 for (left) spring (February-March) and (right) autumn (October-November). The ICESat data are averaged over autumn 2004-2008 and spring 2003-2007, while the WACCM6 and CAM6 data are averaged over 2003-2008 for both spring and autumn. The WACCM6 and CAM6 ensemble averages of all available members are shown in panels (b)-(d) and show only the regions with co-located ICESat data.

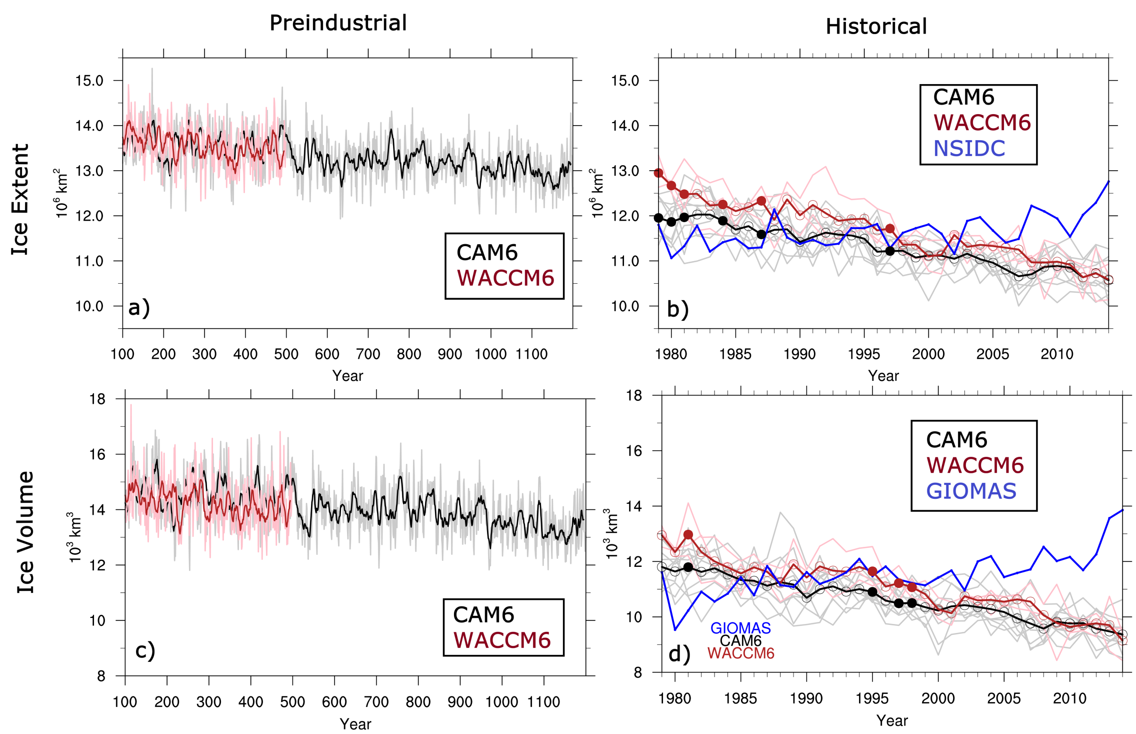

Figure 6: As in Figure 1 (a) – (d), but for the Southern Hemisphere.

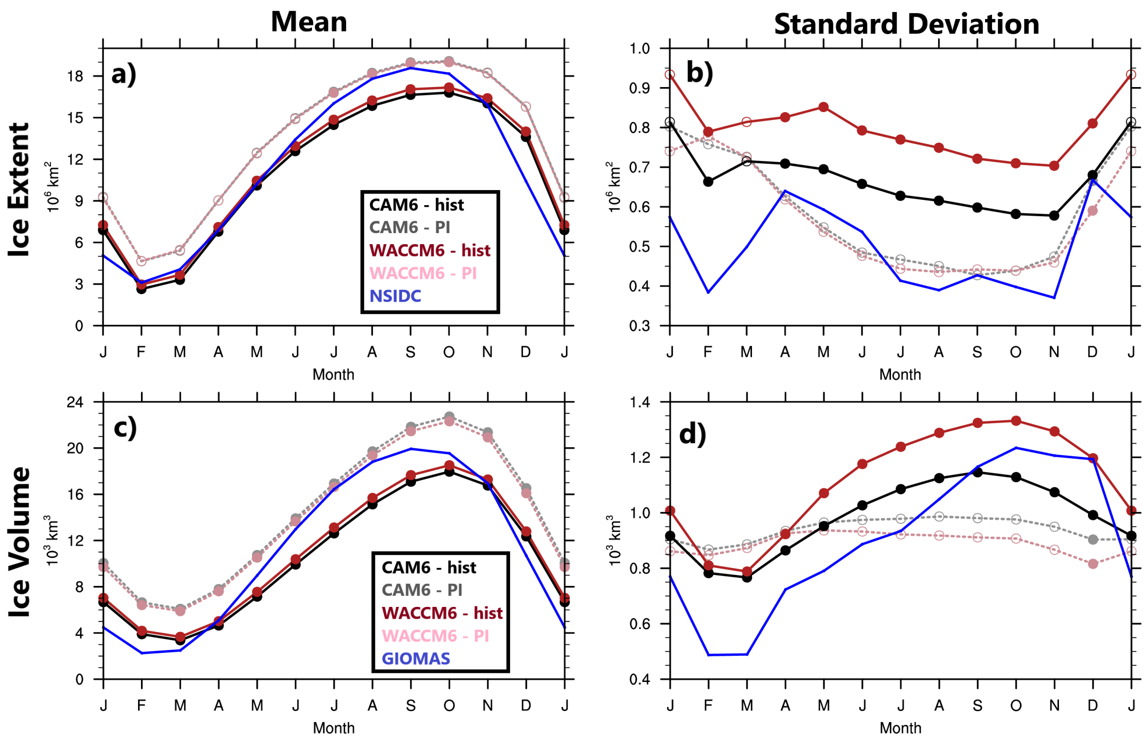

Figure 7: As in Figure 2, but for the Southern Hemisphere.

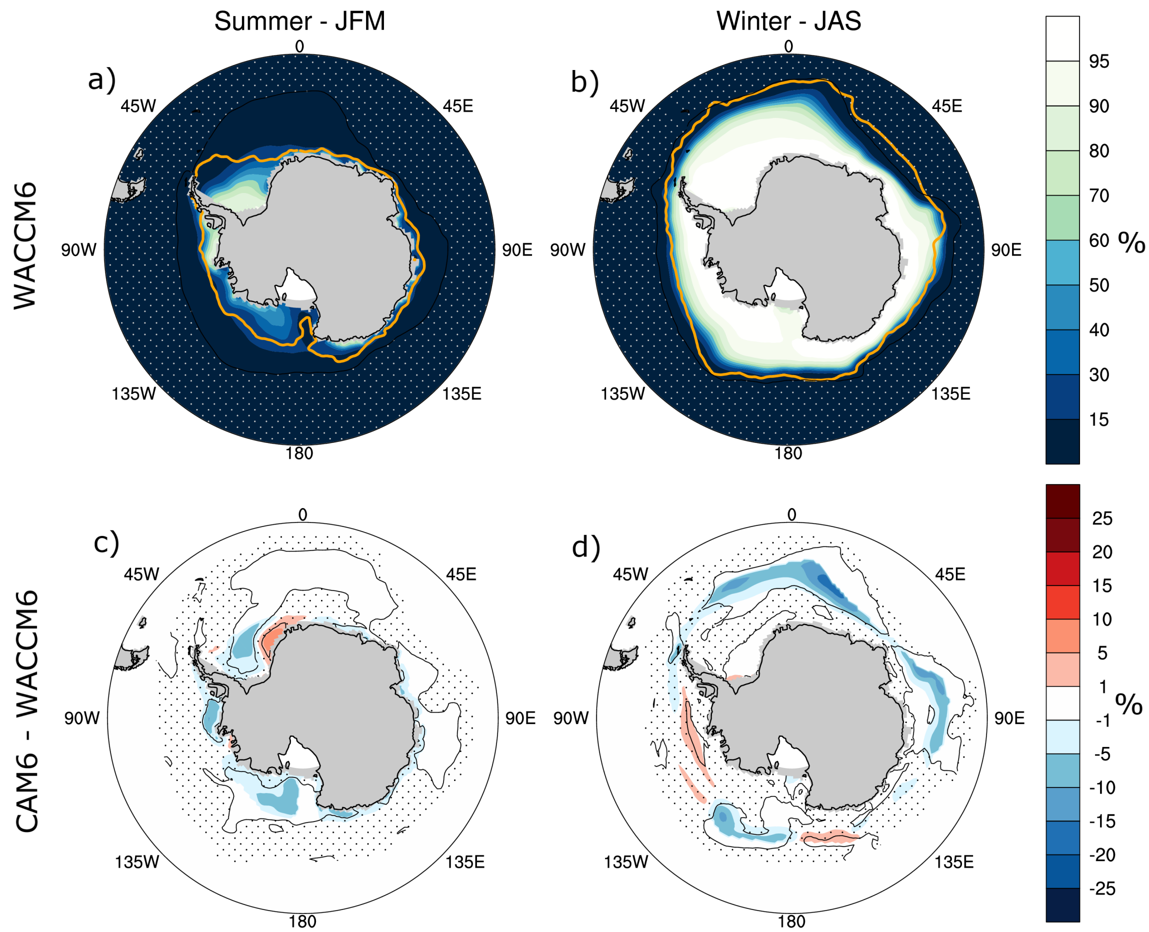

Figure 8: As in Figure 3, but for the Southern Hemisphere.

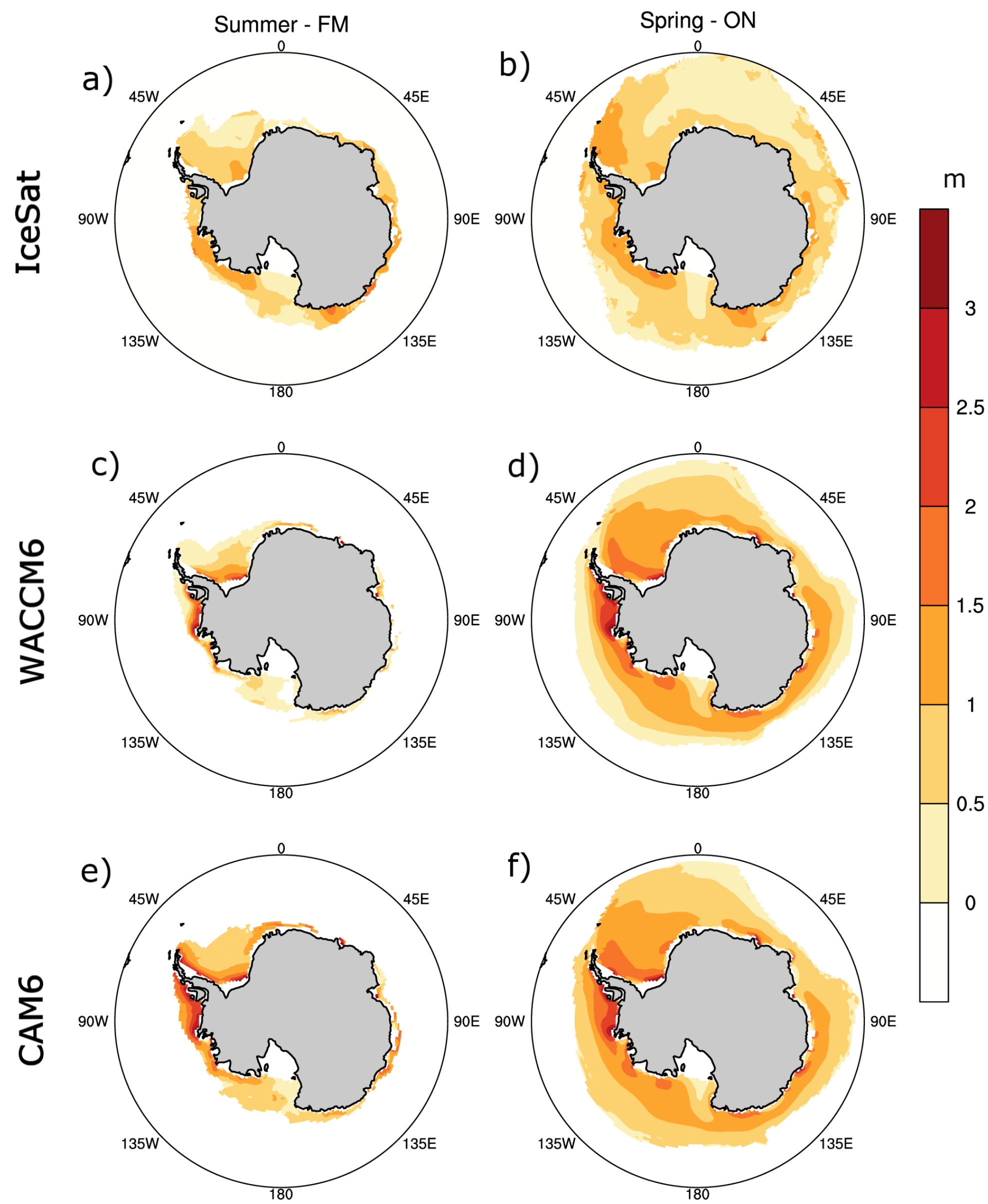

Figure 9: Sea ice thickness (m) from (a),(b) ICESat data (Kurtz and Markus 2012), (c),(d) WACCM6, and (e),(f) CAM6 for (left) summer (February-March) and (right) spring (October-November). The ICESat data are averaged over summer 2004-2008 and spring 2003-2007, while the WACCM6 and CAM6 data are averaged over 2003-2008 for both spring and summer. The WACCM6 and CAM6 ensemble averages of all available members are shown in panels (b)-(d) and show only the regions with sea ice concentration above 50% to be consistent with the ICESat data.

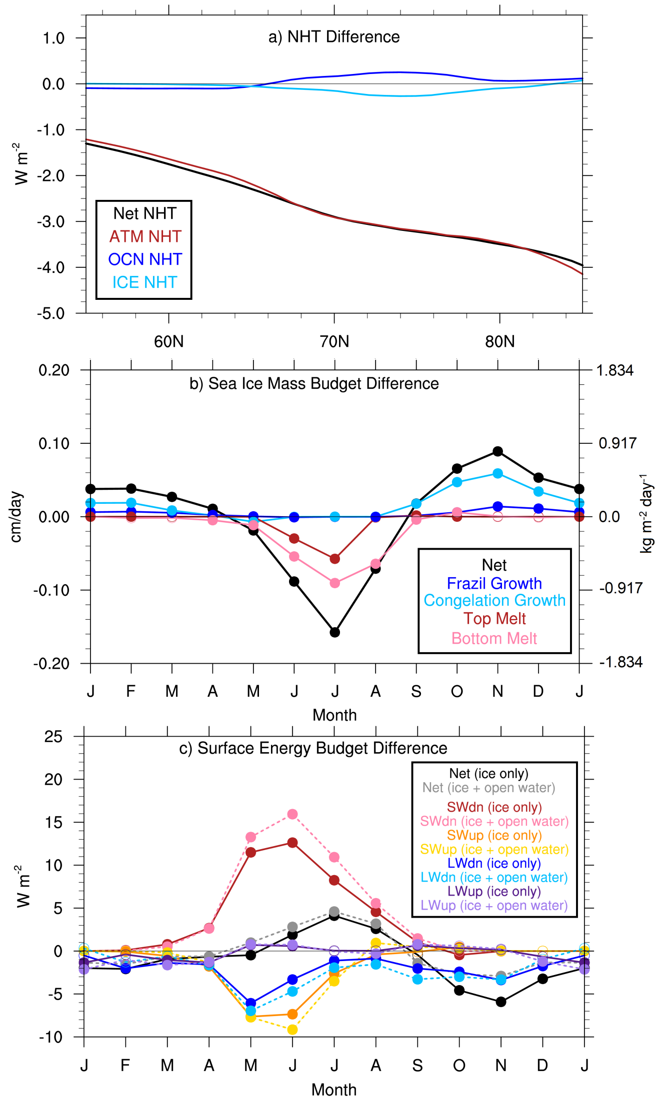

Figure 10: Difference (CAM6-WACCM6) in (a) zonal mean northward heat transport divided by the surface area north of the given latitude (W m^{-2}) and component terms, (b) net sea ice mass budget (cm day^{-1} left axis; kg m^{-2} day^{-1} right axis) and component terms, and (c) net surface energy budget (W m^{-2}) and radiative component terms over sea ice only (solid; dark colors) and over the ocean and ice surface (dashed; light colors). In (b),(c) large solid circles indicate when the CAM6 and WACCM6 values are different at the 95% significance level. The CAM6 and WACCM6 means are calculated over the PI years 100-500.

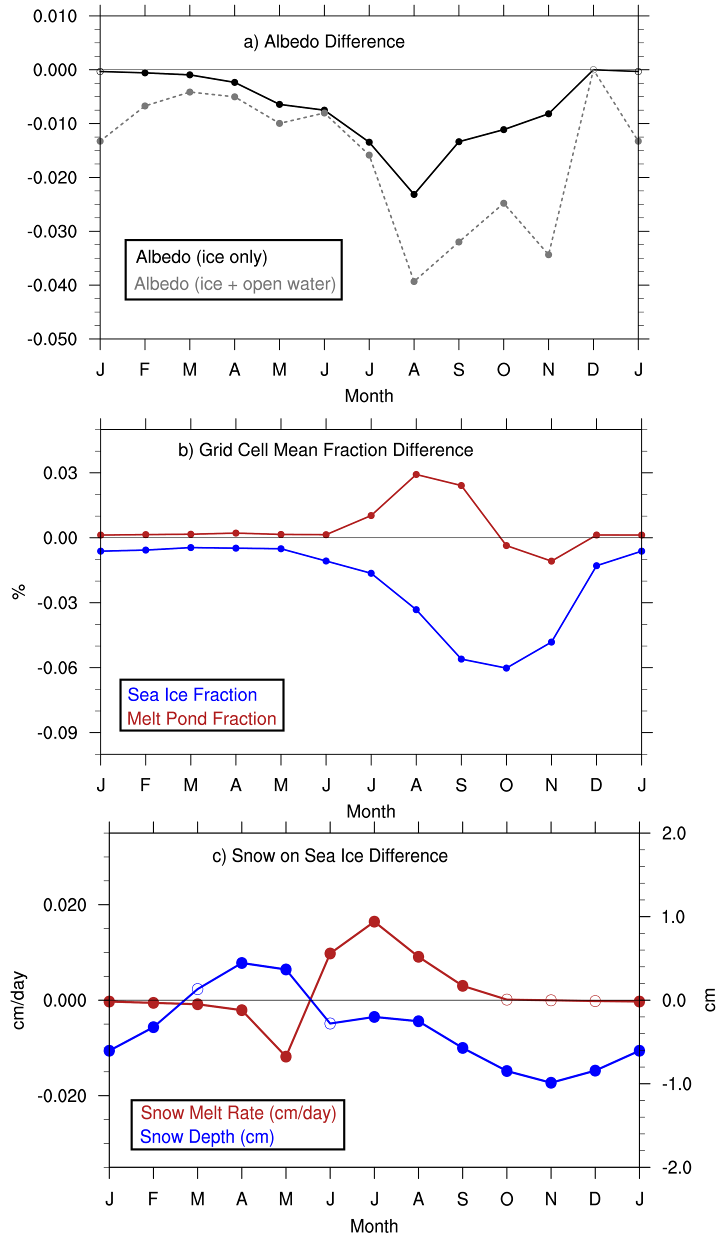

Figure 11: Monthly mean difference (CAM6-WACCM6) in (a) surface albedo over sea ice only (solid; black) and over the whole surface (dashed; grey), (b) fraction (%) of grid cell covered by sea ice (blue) and melt ponds (red), and (c) the melt rate for snow on sea ice (red; cm/day) and depth of snow on sea ice (blue; cm). Large solid circles indicate when the CAM6 and WACCM6 values are different at the 95% significance level. The CAM6 and WACCM6 means are calculated over the PI years 100-500.

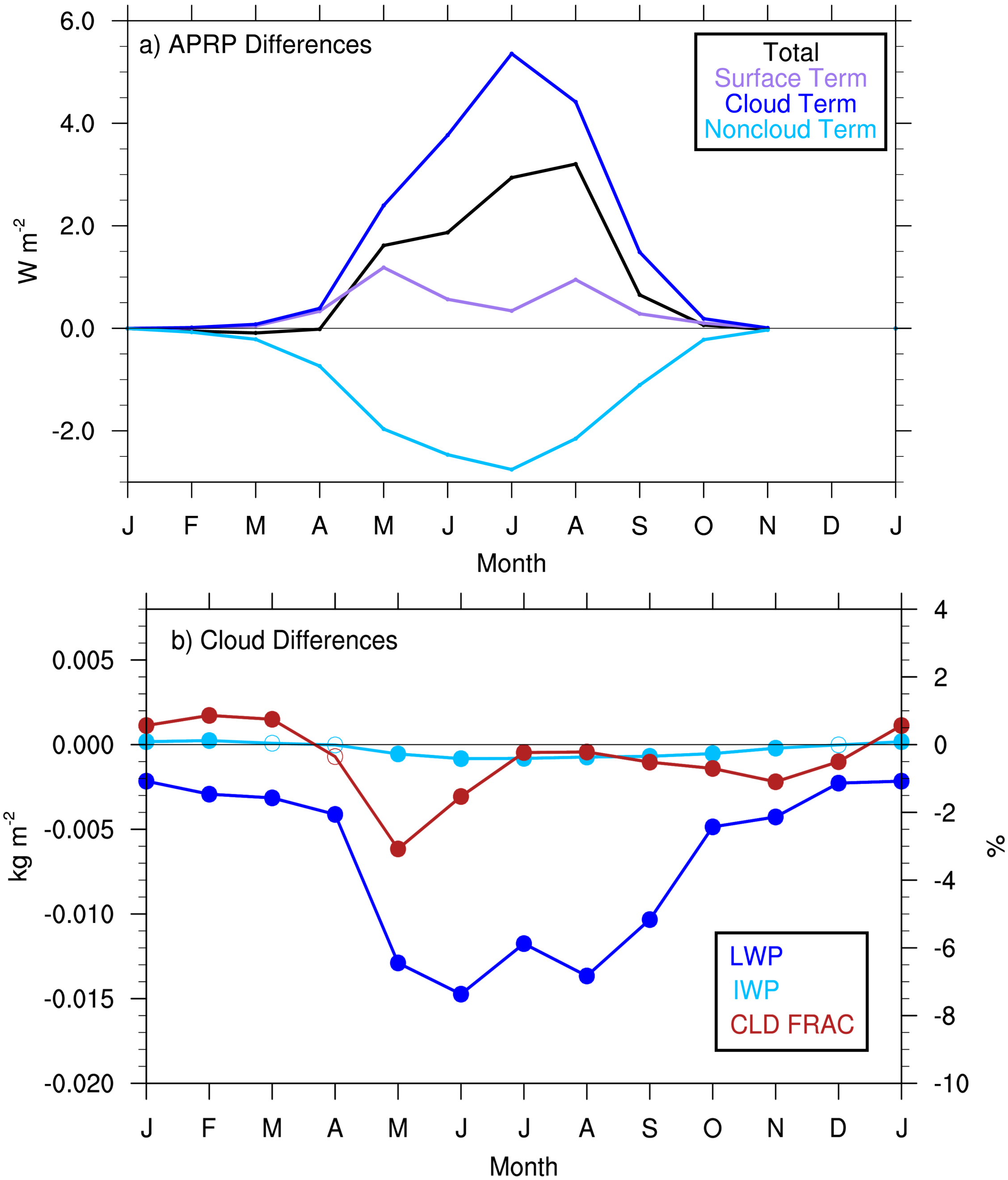

Figure 12: Monthly mean difference (CAM6-WACCM6) over 70-90°N for (a) mean APRP shortwave feedback terms (W m^{-2}) and (b) cloud fraction (%) and cloud liquid water path and ice water path (kg m^{-2}). Large solid circles indicate when the CAM6 and WACCM6 values are different at the 95% significance level. The CAM6 and WACCM6 means are calculated over the PI years 100-500.

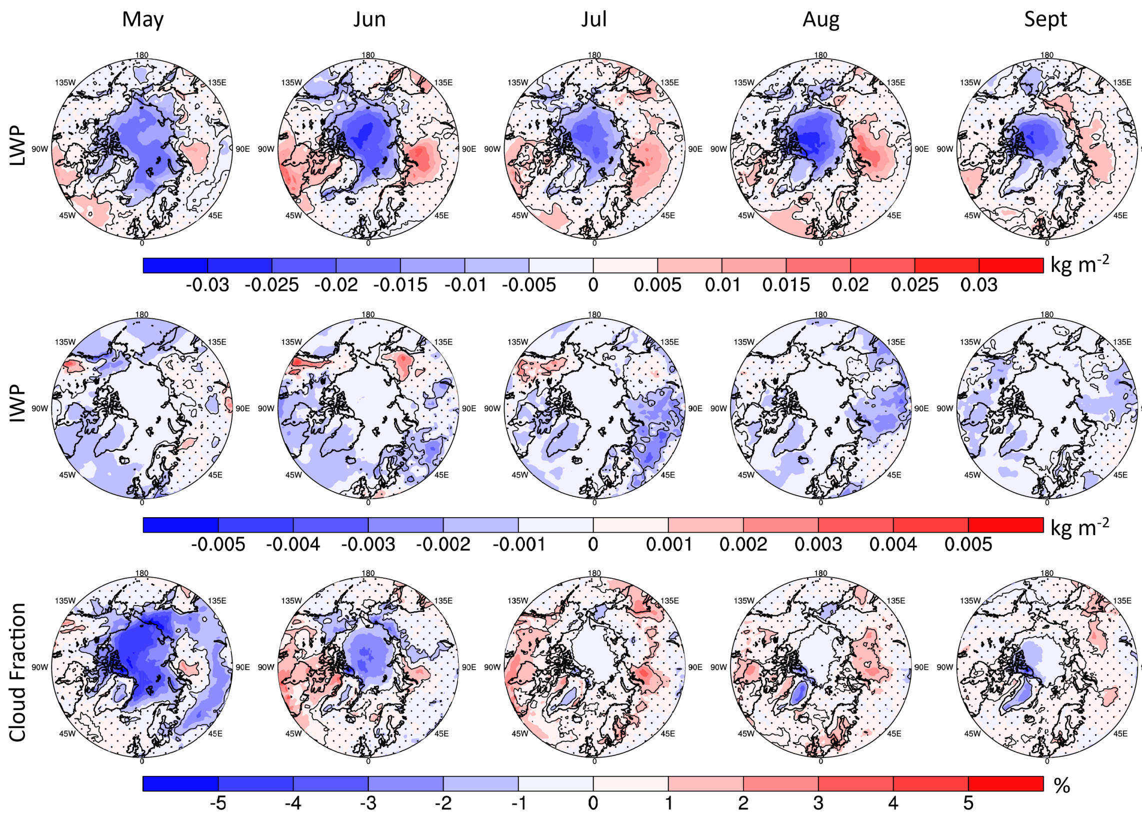

Figure 13. Monthly mean difference (CAM6-WACCM6) for (top row) cloud LWP (kg m^{-2}), (middle row) cloud IWP (kg m^{-2}), and (bottom row) cloud fraction (%) for the months of May, June, July, August, and September. Stippling indicates locations where the CAM6 and WACCM6 values are not different at the 95% significance level. The CAM6 and WACCM6 means are calculated over the PI years 100-500.

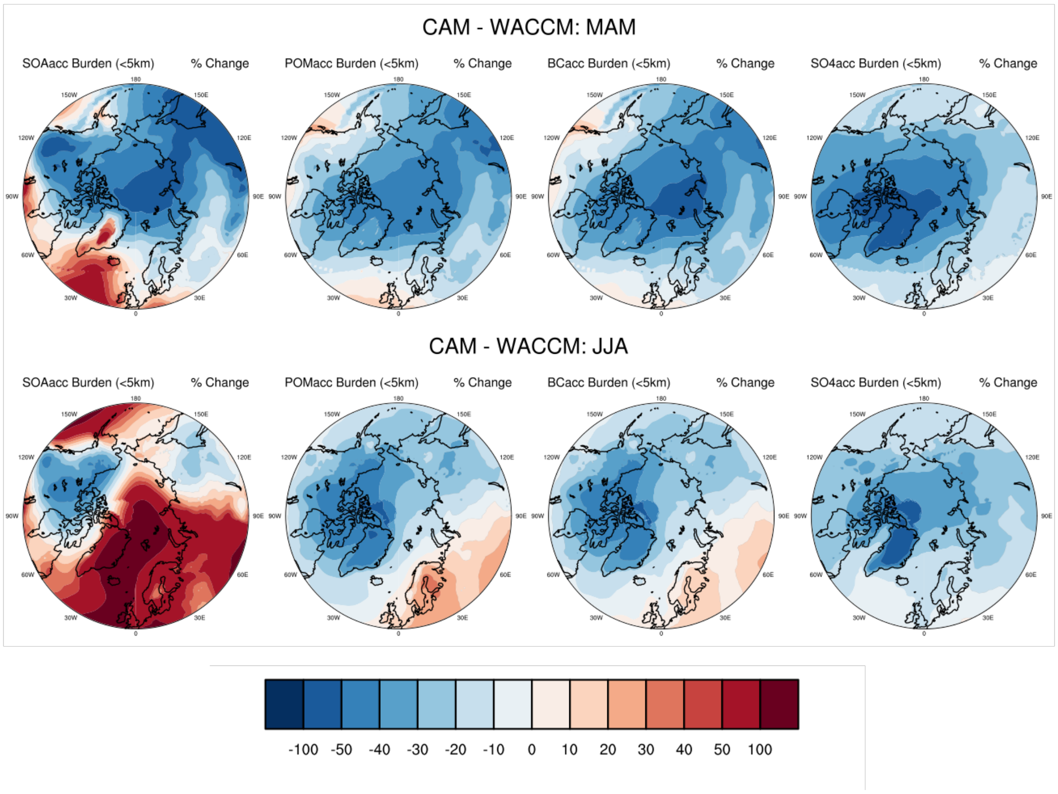

Figure 14: Percent change in (CAM6-WACCM6) Arctic aerosol burden for (top row) spring (March-May) and (bottom row) summer (June-August). Aerosols shown are (left column) Secondary Organic Aerosols, (left-middle column) Primary Organic Matter, (right-middle column) Black Carbon, and (right column) Sulfates.

References

Alexander, M. A. (2004). The Atmospheric Response to Realistic Arctic Sea Ice Anomalies in an AGCM during Winter. *JOURNAL OF CLIMATE*, *17*, 16. https://doi.org/10.1175/1520-0442(2004)017<0890:TARTRA>2.0.CO;2

Bailey, D. A., Holland, M. M., DuVivier, A. K., Hunke, E. C., & Turner, A. K. (2020). Impact of Sea Ice Thermodynamics in the CESM2 sea ice component. *Journal of Geophysical Research: Ocean*.

Barnes, E. A., & Screen, J. A. (2015). The impact of Arctic warming on the midlatitude jet-stream: Can it? Has it? Will it? *Wiley Interdisciplinary Reviews: Climate Change*, *6*(3), 277–286. https://doi.org/10.1002/wcc.337

Barnhart, K. R., Miller, C. R., Overeem, I., & Kay, J. E. (2015). Mapping the future expansion of Arctic open water. *Nature Climate Change*, *6*(3), 280–285. https://doi.org/10.1038/nclimate2848

Bitz, C. M., Holland, M. M., Hunke, E. C., & Moritz, R. E. (2005). Maintenance of the Sea-Ice Edge. *Journal of Climate*, *18*(15), 2903–2921. https://doi.org/10.1175/JCLI3428.1

Boisvert, L. N., & Stroeve, J. C. (2015). The Arctic is becoming warmer and wetter as revealed by the Atmospheric Infrared Sounder. *Geophysical Research Letters*, *42*(11), 4439–4446. https://doi.org/10.1002/2015GL063775

Comiso, J. C. (2000). Bootstrap sea ice concentrations from Nimbus-7 SSMR and DMSP SSM/I-SSMIS, version 2. Boulder, Colorado USA: National Snow and Ice Data Center. Digital media. Retrieved from http://nsidc.org/data/nsidc-0079

Danabasoglu, G., Lamarque, J. -F., Bacmeister, J., Bailey, D. A., DuVivier, A. K., Edwards, J., et al. (2020). The Community Earth System Model Version 2 (CESM2). *Journal of Advances in Modeling Earth Systems*, *12*(2). https://doi.org/10.1029/2019MS001916

Danabasoglu, Gokhan, Bates, S. C., Briegleb, B. P., Jayne, S. R., Jochum, M., Large, W. G., et al. (2012). The CCSM4 Ocean Component. *Journal of Climate*, *25*(5), 1361–1389. https://doi.org/10.1175/JCLI-D-11-00091.1

DeRepentigny, P., Tremblay, L. B., Newton, R., & Pfirman, S. (2016). Patterns of Sea Ice Retreat in the Transition to a Seasonally Ice-Free Arctic. *Journal of Climate*, *29*(19), 6993–7008. https://doi.org/10.1175/JCLI-D-15-0733.1

DeRepentigny, P., Jahn, A., Holland, M. M., & Smith, A. (2020). Arctic Sea Ice in Two Configurations of the Community Earth System Model Version 2 (CESM2) During the 20th and 21st Centuries. *Journal of Geophysical Research: Oceans*. https://doi.org/10.1029/2020JC016133

Deser, C., Sun, L., Tomas, R. A., & Screen, J. (2016). Does ocean coupling matter for the northern extratropical response to projected Arctic sea ice loss? *Geophysical Research Letters*, *43*(5), 2149–2157. https://doi.org/10.1002/2016GL067792

Fetterer, F., Knowles, K., Meier, W. N., Savoie, M. H., & Windnagel, A. K. (2017). Sea Ice Index, Version 3. *NSIDC: National Snow and Ice Data Center. Boulder, Colorado USA*. https://doi.org/10.7265/N5K072F8

Gettelman, A., Mills, M. J., Kinnison, D., Garcia, R., Smith, A., Marsh, D., et al. (2019). The Whole Atmosphere Community Climate Model Version 6 (WACCM6). *Journal of Geophysical Research-Atmospheres*.

Goosse, H., Arzel, O., Bitz, C. M., de Montety, A., & Vancoppenolle, M. (2009). Increased variability of the Arctic summer ice extent in a warmer climate. *Geophysical Research Letters*, *36*(23), L23702. https://doi.org/10.1029/2009GL040546

Goosse, Hugues, Kay, J. E., Armour, K. C., Bodas-Salcedo, A., Chepfer, H., Docquier, D., et al. (2018). Quantifying climate feedbacks in polar regions. *Nature Communications*, *9*(1), 1919. https://doi.org/10.1038/s41467-018-04173-0

Hobbs, W. R., Bindoff, N. L., & Raphael, M. N. (2015). New perspectives on observed and simulated Antarctic Sea ice extent trends using optimal fingerprinting techniques. *Journal of Climate*, *28*(4), 1543–1560.

Holland, M. M., Bitz, C. M., Hunke, E. C., Lipscomb, W. H., & Schramm, J. L. (2006). Influence of the Sea Ice Thickness Distribution on Polar Climate in CCSM3. *Journal of Climate*, *19*(11), 2398–2414. https://doi.org/10.1175/JCLI3751.1

Holland, M. M., Bitz, C. M., Tremblay, L.-B., & Bailey, D. A. (2008). The Role of Natural Versus Forced Change in Future Rapid Summer Arctic Ice Loss. In E. T. DeWeaver, C. M. Bitz, & L.-B. Tremblay (Eds.), *Geophysical Monograph Series* (pp. 133–150). Washington, D.C.: American Geophysical Union. https://doi.org/10.1029/180GM10

Huang, Y., Dong, X., Bailey, D. A., Holland, M. M., Xi, B., DuVivier, A. K., et al. (2019). Thicker clouds and accelerated Arctic sea ice decline: The atmosphere-sea ice interactions in spring. *Geophysical Research Letters*, 2019GL082791. https://doi.org/10.1029/2019GL082791

Hunke, E. C., Hebert, D. A., & Lecomte, O. (2013). Level-ice melt ponds in the Los Alamos sea ice model, CICE. *Ocean Modelling*, *71*, 26–42. https://doi.org/10.1016/j.ocemod.2012.11.008

Hunke, E. C., Lipscomb, W. H., Turner, A. K., Jeffery, N., & Elliott, S. (2015). CICE: the Los Alamos Sea Ice Model Documentation and Software User's Manual Version 5.1 LA-CC-012. Retrieved from http://oceans11. lanl.gov/trac/CICE/wiki/SourceCode

Hunter, C. M., Caswell, H., Runge, M. C., Regehr, E. V., Amstrup, S. C., & Stirling, I. (2010). Climate change threatens polar bear populations: a stochastic demographic analysis, *91*(10), 15.

Jahn, A., Sterling, K., Holland, M. M., Kay, J. E., Maslanik, J. A., Bitz, C. M., et al. (2012). Late-Twentieth-Century Simulation of Arctic Sea Ice and Ocean Properties in the CCSM4. *Journal of Climate*, *25*(5), 1431–1452. https://doi.org/10.1175/JCLI-D-11-00201.1

Jahn, A., Kay, J. E., Holland, M. M., & Hall, D. M. (2016). How predictable is the timing of a summer ice-free Arctic? *Geophysical Research Letters*, *43*(17), 9113–9120. https://doi.org/10.1002/2016GL070067

Jenouvrier, S., Holland, M., Stroeve, J., Serreze, M., Barbraud, C., Weimerskirch, H., & Caswell, H. (2014). Projected continent-wide declines of the emperor penguin under climate change. *NATURE CLIMATE CHANGE*, *4*, 4.

Kalnay, E., Kanamitsu, M., Kistler, R., Collins, W., Deaven, D., Gandin, L., et al. (1996). The NCEP/NCAR 40-Year Reanalysis Project. *Bulletin of the American Meteorological Society*, *77*(3), 437–471. https://doi.org/10.1175/1520-0477(1996)077<0437:TNYRP>2.0.CO;2

Kay, J. E., & Gettelman, A. (2009). Cloud influence on and response to seasonal Arctic sea ice loss. *Journal of Geophysical Research*, *114*(D18). https://doi.org/10.1029/2009JD011773

Kay, J. E., Holland, M. M., & Jahn, A. (2011). Inter-annual to multi-decadal Arctic sea ice extent trends in a warming world. *Geophysical Research Letters*, *38*(15). https://doi.org/10.1029/2011GL048008

Kay, J. E., Raeder, K., Gettelman, A., & Anderson, J. (2011). The Boundary Layer Response to Recent Arctic Sea Ice Loss and Implications for High-Latitude Climate Feedbacks. *Journal of Climate*, *24*(2), 428–447. https://doi.org/10.1175/2010JCLI3651.1

Kay, J. E., Holland, M. M., Bitz, C. M., Blanchard-Wrigglesworth, E., Gettelman, A., Conley, A., & Bailey, D. (2012). The Influence of Local Feedbacks and Northward Heat Transport on the Equilibrium Arctic Climate Response to Increased Greenhouse Gas Forcing. *Journal of Climate*, *25*(16), 5433–5450. https://doi.org/10.1175/JCLI-D-11-00622.1

Kovacs, K. M., Lydersen, C., Overland, J. E., & Moore, S. E. (2011). Impacts of changing sea-ice conditions on Arctic marine mammals, 14.

Kurtz, N. T., & Markus, T. (2012). Satellite observations of Antarctic sea ice thickness and volume. *Journal of Geophysical Research: Oceans*, *117*(C8), n/a-n/a. https://doi.org/10.1029/2012JC008141

Kwok, R. (2018). Arctic sea ice thickness, volume, and multiyear ice coverage: losses and coupled variability (1958–2018). *Environmental Research Letters*, *13*(10), 105005. https://doi.org/10.1088/1748-9326/aae3ec

Kwok, R., Cunningham, G. F., Wensnahan, M., Rigor, I., Zwally, H. J., & Yi, D. (2009). Thinning and volume loss of the Arctic Ocean sea ice cover: 2003–2008. *Journal of Geophysical Research: Oceans*, *114*(C7), C07005. https://doi.org/10.1029/2009JC005312

Labe, Z., Magnusdottir, G., & Stern, H. (2018). Variability of Arctic Sea Ice Thickness Using PIOMAS and the CESM Large Ensemble. *Journal of Climate*, *31*(8), 3233–3247. https://doi.org/10.1175/JCLI-D-17-0436.1

Landrum, L., Holland, M. M., Schneider, D. P., & Hunke, E. (2012). Antarctic Sea Ice Climatology, Variability, and Late Twentieth-Century Change in CCSM4. *Journal of Climate*, *25*(14), 4817–4838. https://doi.org/10.1175/JCLI-D-11-00289.1

Laxon, S. W., Giles, K. A., Ridout, A. L., Wingham, D. J., Willatt, R., Cullen, R., et al. (2013). CryoSat-2 estimates of Arctic sea ice thickness and volume. *Geophysical Research Letters*, *40*(4), 732–737. https://doi.org/10.1002/grl.50193

Lindsay, R., & Schweiger, A. (2015). Arctic sea ice thickness loss determined using subsurface, aircraft, and satellite observations. *The Cryosphere*, *9*(1), 269–283. https://doi.org/10.5194/tc-9-269-2015

Liu, Y., Key, J. R., Wang, X., & Tschudi, M. (2020). Multidecadal Arctic sea ice thickness and volume derived from ice age. *The Cryosphere*, *14*(4), 1325–1345. https://doi.org/10.5194/tc-14-1325-2020

Mahlstein, I., Gent, P. R., & Solomon, S. (2013). Historical Antarctic mean sea ice area, sea ice trends, and winds in CMIP5 simulations. *Journal of Geophysical Research: Atmospheres*, *118*(11), 5105–5110. https://doi.org/10.1002/jgrd.50443

Maykut, G. A. (1982). Large-scale heat exchange and ice production in the central Arctic. *Journal of Geophysical Research*, *87*(C10), 7971. https://doi.org/10.1029/JC087iC10p07971

McIlhattan, E. A., Kay, J. E., & L'Ecuyer, T. S. (2020). Arctic Clouds and Precipitation in the Community Earth System Model Version 2. *Journal of Geophysical Research: Atmospheres*.

Meehl, G. A., Arblaster, J. M., Chung, C. T. Y., Holland, M. M., DuVivier, A., Thompson, L., et al. (2019). Sustained ocean changes contributed to sudden Antarctic sea ice retreat in late 2016. *Nature Communications*, *10*(1). https://doi.org/10.1038/s41467-018-07865-9

Meredith, M., Sommerkorn, M., Cassotta, S., Derksen, C., Ekaykin, A., Hollowed, A., et al. (2019). Chapter 3: Polar Regions. In H. O. Portner, D. C. Roberts, V.

Masson-Delmotte, P. Zhai, M. Tignor, E. Poloczanska, et al. (Eds.), *IPCC Special Report on the Ocean and Cryosphere in a Changing Climate*.

Mills, M. J., Richter, J. H., Tilmes, S., Kravitz, B., MacMartin, D. G., Glanville, A. A., et al. (2017). Radiative and Chemical Response to Interactive Stratospheric Sulfate Aerosols in Fully Coupled CESM1(WACCM). *Journal of Geophysical Research: Atmospheres*, *122*(23), 13,061-13,078. https://doi.org/10.1002/2017JD027006

Moon, T. A., Overeem, I., Druckenmiller, M., Holland, M., Huntington, H., Kling, G., et al. (2019). The Expanding Footprint of Rapid Arctic Change. *Earth's Future*, *7*(3), 212–218. https://doi.org/10.1029/2018EF001088

Morrison, A., Kay, J. E., Chepfer, H., Guzman, R., & Yettella, V. (2018). Isolating the Liquid Cloud Response to Recent Arctic Sea Ice Variability Using Spaceborne Lidar Observations. *Journal of Geophysical Research: Atmospheres*, *123*(1), 473–490. https://doi.org/10.1002/2017JD027248

Morrison, A., Kay, J. E., Frey, W. R., Chepfer, H., & Guzman, R. (2019). Cloud Response to Arctic Sea Ice Loss and Implications for Future Feedbacks in the CESM1 Climate Model. *Journal of Geophysical Research: Atmospheres*. https://doi.org/10.1029/2018JD029142

Notz, D., Jahn, A., Holland, M., Hunke, E., Massonnet, F., Stroeve, J., et al. (2016). The CMIP6 Sea-Ice Model Intercomparison Project (SIMIP): understanding sea ice through climate-model simulations. *Geoscientific Model Development*, *9*(9), 3427–3446. https://doi.org/10.5194/gmd-9-3427-2016

Parkinson, C. L. (2019). A 40-y record reveals gradual Antarctic sea ice increases followed by decreases at rates far exceeding the rates seen in the Arctic. *Proceedings of the National Academy of Sciences*, *116*(29), 14414–14423. https://doi.org/10.1073/pnas.1906556116

Perovich, D. K., Light, B., Eicken, H., Jones, K. F., Runciman, K., & Nghiem, S. V. (2007). Increasing solar heating of the Arctic Ocean and adjacent seas, 1979–2005: Attribution and role in the ice-albedo feedback. *Geophysical Research Letters*, *34*(19), L19505. https://doi.org/10.1029/2007GL031480

Pithan, F., & Mauritsen, T. (2014). Arctic amplification dominated by temperature feedbacks in contemporary climate models. *Nature Geoscience*, *7*(3), 181–184. https://doi.org/10.1038/ngeo2071

Polvani, L. M., & Smith, K. L. (2013). Can natural variability explain observed Antarctic sea ice trends? New modeling evidence from CMIP5. *Geophysical Research Letters*, *40*(12), 3195–3199. https://doi.org/10.1002/grl.50578

Raphael, M. N., Handcock, M. S., Holland, M. M., & Landrum, L. L. (2020). An assessment of the temporal variability in the annual cycle of daily Antarctic sea ice in the NCAR Community Earth System Model, Version 2: A comparison of the historical runs with observations. *Journal of Geophysical Research: Oceans*.

Richter-Menge, J. A., Osborne, E., Druckenmiller, M., & Jeffries, M. O. (Eds.). (2019). The Arctic [in “State of the Climate in 2018”]. *Bulletin of the American Meteorological Society*, *100*(9), S141–S168.

Schweiger, A., Lindsay, R., Zhang, J., Steele, M., Stern, H., & Kwok, R. (2011). Uncertainty in modeled Arctic sea ice volume. *Journal of Geophysical Research*, *116*, C00D06. https://doi.org/10.1029/2011JC007084

Shu, Q., Song, Z., & Qiao, F. (2015). Assessment of sea ice simulations in the CMIP5 models. *The Cryosphere*, *9*(1), 399–409. https://doi.org/10.5194/tc-9-399-2015

Shupe, M. D., & Intrieri, J. M. (2004). Cloud radiative forcing of the Arctic surface: The influence of cloud properties, surface albedo, and solar zenith angle. *Journal of Climate*, *17*(3), 616–628. http://dx.doi.org/10.1175/1520-0442(2004)017<0616:CRFOTA>2.0.CO;2

Singh, H. K. A., Landrum, L., & Holland, M. M. (2020). An Overview of Antarctic Sea Ice in the CESM2: Analysis of the Seasonal Cycle, Predictability, and Atmosphere-Ocean-Ice Interactions. *JAMES*.

Smith, R., Jones, P., Briegleb, B., Bryan, F., Danabasoglu, G., Dennis, J., et al. (2010). The Parallel Ocean Program (POP) Reference Manual Ocean Component of the Community Climate System Model (CCSM) and Community Earth System Model (CESM). *Rep. LAUR-01853*, *141*. Retrieved from https://ccsm.ucar.edu/models/cesm1.2/pop2/doc/sci/POPRefManual.pdf

Stroeve, J., Barrett, A., Serreze, M., & Schweiger, A. (2014). Using records from submarine, aircraft and satellites to evaluate climate model simulations of Arctic sea ice thickness. *The Cryosphere*, *8*(5), 1839–1854. https://doi.org/10.5194/tc-8-1839-2014

Stroeve, Julienne, & Notz, D. (2018). Changing state of Arctic sea ice across all seasons. *Environmental Research Letters*, *13*(10), 103001. https://doi.org/10.1088/1748-9326/aade56

Stuecker, M. F., Bitz, C. M., & Armour, K. C. (2017). Conditions leading to the unprecedented low Antarctic sea ice extent during the 2016 austral spring season. *Geophysical Research Letters*. https://doi.org/10.1002/2017GL074691

Swart, N. C., Fyfe, J. C., Hawkins, E., Kay, J. E., & Jahn, A. (2015). Influence of internal variability on Arctic sea-ice trends. *Nature Climate Change*, *5*(2), 86–89. https://doi.org/10.1038/nclimate2483

Taylor, K. E., Crucifix, M., Braconnot, P., Hewitt, C. D., Doutriaux, C., Broccoli, A. J., et al. (2007). Estimating Shortwave Radiative Forcing and Response in Climate Models. *Journal of Climate*, *20*(11), 2530–2543. https://doi.org/10.1175/JCLI4143.1

Tilmes, S., Hodzic, A., Emmons, L. K., Mills, M. J., Gettelman, A., Kinnison, D. E., et al. (2019). Climate Forcing and Trends of Organic Aerosols in the Community Earth System Model (CESM2). *Journal of Advances in Modeling Earth Systems*, *11*(12), 4323–4351. https://doi.org/10.1029/2019MS001827

Tschudi, M. A., Meier, W. N., Stewart, J. S., Fowler, C., & Maslanik, J. (2019). EASE-Grid Sea Ice Age, Version 4. Retrieved from https://doi.org/10.5067/UTAV7490FEPB

Turner, A. K., & Hunke, E. C. (2015). Impacts of a mushy-layer thermodynamic approach in global sea-ice simulations using the CICE sea-ice model. *Journal* *of Geophysical Research: Oceans*, *120*(2), 1253–1275. https://doi.org/10.1002/2014JC010358

Turner, J., Bracegirdle, T. J., Phillips, T., Marshall, G. J., & Hosking, J. S. (2013). An Initial Assessment of Antarctic Sea Ice Extent in the CMIP5 Models. *Journal of Climate*, *26*(5), 1473–1484. https://doi.org/10.1175/JCLI-D-12-00068.1

Turner, J., Phillips, T., Marshall, G. J., Hosking, J. S., Pope, J. O., Bracegirdle, T. J., & Deb, P. (2017). Unprecedented springtime retreat of Antarctic sea ice in 2016: The 2016 Antarctic Sea Ice Retreat. *Geophysical Research Letters*, *44*(13), 6868–6875. https://doi.org/10.1002/2017GL073656

Wang, Z., Turner, J., Wu, Y., & Liu, C. (2019). Rapid Decline of Total Antarctic Sea Ice Extent during 2014–16 Controlled by Wind-Driven Sea Ice Drift. *Journal of Climate*, *32*(17), 5381–5395. https://doi.org/10.1175/JCLI-D-18-0635.1

West, A., Collins, M., Blockley, E., Ridley, J., & Bodas-Salcedo, A. (2019). Induced surface fluxes: a new framework for attributing Arctic sea ice volume balance biases to specific model errors. *The Cryosphere*, *13*(7), 2001–2022. https://doi.org/10.5194/tc-13-2001-2019

Zhang, J., & Rothrock, D. A. (2003). Modeling Global Sea Ice with a Thickness and Enthalpy Distribution Model in Generalized Curvilinear Coordinates. *MONTHLY WEATHER REVIEW*, *131*, 17.